POLITECNICO DI TORINO
Repository ISTITUZIONALE

Machine Precision Evaluation of Singular and Nearly Singular Potential Integrals by Use of Gauss Quadrature Formulas for Rational Functions

*Original*
Machine Precision Evaluation of Singular and Nearly Singular Potential Integrals by Use of Gauss Quadrature Formulas for Rational Functions / Graglia, R., Lombardi, G.. - In: IEEE TRANSACTIONS ON ANTENNAS AND PROPAGATION. - ISSN 0018-926X. - STAMPA. - 56:4(2008), pp. 981-998. [10.1109/TAP.2008.919181]

*Availability:*
This version is available at: 11583/1513279 since:

*Publisher:*
IEEE

*Published*
DOI:10.1109/TAP.2008.919181

*Terms of use:*

This article is made available under terms and conditions as specified in the corresponding bibliographic description in the repository

*Publisher copyright*

(Article begins on next page)

28 November 2026

# Machine Precision Evaluation of Singular and Nearly Singular Potential Integrals by Use of Gauss Quadrature Formulas for Rational Functions

Roberto D. Graglia, *Fellow, IEEE*, and Guido Lombardi, *Member, IEEE*

***Abstract*—A new technique for machine precision evaluation of singular and nearly singular potential integrals with $1/R$ singularities is presented. The numerical quadrature scheme is based on a new rational expression for the integrands, obtained by a cancellation procedure. In particular, by using library routines for Gauss quadrature of rational functions readily available in the literature, this new expression permits the exact numerical integration of singular static potentials associated with polynomial source distributions. The rules to achieve the desired numerical accuracy for singular and nearly singular static and dynamic potential integrals are presented and discussed, and several numerical examples are provided.**

***Index Terms*—Boundary element methods, finite element methods, finite volume methods, integral equations, method of moment (MoM).**

## I. Introduction

POTENTIAL integrals with unbounded singular kernels arise in the moment-method solution of the integral equations of electromagnetism whenever the source and the testing subdomain coincide, that is, in the so-called self-term case. The integrals become nearly singular if the source and testing subdomains are very close to each other, but do not overlap. All these integrals are usually computed by the singularity cancellation [1]–[9] or the singularity subtraction method [10]–[19], with the near-singular case particularly considered in [1], [6]–[9], [14], [20]–[22]. The cancellation method is based on variable transformations whose Jacobian cancels out the singularity of the integral kernel. The superiority of the cancellation method with respect to the subtraction method is established in [1]. Despite its convenience, however, the technique in [1] does not permit one to anticipate the precision of the numerical results, even in the simpler case of static potential integrals, and does not discuss reasons for the higher degree of difficulty inherent in the near-singular case.

Due to the reduced cost and increased computation speed of modern computers, the time is now ripe for machine precision evaluation of potential integrals. This paper describes a new numerical technique to compute singular and nearly singular potential integrals with machine precision; above all, it explains how to obtain it and why it is not possible to predict the precision of the other existing integration techniques.

The most recent advances in the area of computational electromagnetics are not adequately represented in many of the previously quoted papers because of their age. In particular, the majority of those papers prefer to redefine the integration domain of the potential integral by rotating and translating the original given domain. Conversely, in this paper, the singularity cancellation is carried out directly by working in the *parent* reference-frame from the outset, thereby using the language and the techniques well known to finite element analysts [23]. With respect to the previous approaches, this has some important advantages that are described in Sections II and III. Section IV then considers potential integrals on surface *elements*, explains the new integration technique and elucidates the difficulties in evaluating near-singular integrals as compared to the singular ones. Our quadrature scheme is based on a new rational representation of the integrands resulting from the presented cancellation procedure. This expression permits the exact numerical integration of the static potentials associated with polynomial source distributions using library routines for Gauss quadrature of rational functions that are readily available in the literature [24]. Integrals on three-dimensional source domains are briefly discussed in Section V, whereas Section VI provides several numerical results for potential integrals on surface elements. Section VI also explains, in considerable detail and with several examples, how to achieve machine precision accuracy for static and dynamic potential integrals. Preliminary results of this work have been reported in [25], [26].

## II. Object and Parent Elements for Computational Electromagnetics

Modern electromagnetic (EM) codes model the geometry of a given problem as the union of subdomains of different but simple geometrical shapes. EM problems are then numerically solved by expanding the unknowns in terms of vector or scalar functions locally defined on these subdomains. The expansion functions are conveniently defined on rectilinear domains of a *parent* space, with all subdomains of the global geometry obtained by properly mapping one or a few parent domains onto the global object-space. In its parent space a domain is described in terms of a set $\xi$ of normalized (dimensionless) parametric

Manuscript received December 5, 2006; revised September 28, 2007. This work was supported by NATO in the framework of the Science for Peace Programme under the grant CBP.MD.SFPP 982376—*Electromagnetic Signature of Edge-Structures for Unexploded Ordnance Detection*.

R. D. Graglia is with the Dipartimento di Elettronica, Politecnico di Torino, 10129 Torino, Italy and also with the ISMB-Instituto Superiore Mario Boella, 10138 Torino, Italy (e-mail: roberto.graglia@polito.it).

G. Lombardi is with the Dipartimento di Elettronica, Politecnico di Torino, 10129 Torino, Italy (e-mail: guido.lombardi@polito.it).

Digital Object Identifier 10.1109/TAP.2008.919181

0018-926X/$25.00 © 2008 IEEE

coordinates $\boldsymbol{\xi} = (\xi_1, \xi_2, \ldots, \xi_\sigma)$; the parent domain is rectilinear even though the corresponding object-space subdomains might be curvilinear. The word *element* indicates a subdomain together with a set of expansion functions and associated degrees of freedom defined on it [27]. However, the term element is often misused to indicate just the subdomain itself, and we are not ourselves faultless on this score.

Several elements were defined and used in previous works. Two-dimensional (2D) triangular and quadrilateral elements, as well as three-dimensional (3D) tetrahedral and brick elements are, for example, discussed in [28], whereas prism and pyramidal elements are given in [29] and [30], respectively. In the following we assume the reader to be comfortable with the definitions given in those papers, and adopt the same notation used there to discuss application of the singularity cancellation method to evaluate potential integrals.

All parametric coordinates are positive inside the element, and every point outside of the element has one or more negative parent coordinates. For nested integration over the element region

$$E_\xi = \{\xi_i | \xi_i \geq 0, \forall i \in [1, \sigma]\} \tag{1}$$

the $\xi$ upper bounds must be obtained explicitly through the dependency relationships (see [28]–[30]), thereby ensuring non-negative coordinates within the integration region.

The number $\sigma$ of parametric coordinates used to describe a given element is the *size* of the element, or equivalently, the size of the set $\boldsymbol{\xi}$. The size of a two-dimensional element is the number of its edges whereas, for three-dimensional elements, the size $\sigma$ is the number of the element faces. The sizes of triangular and quadrilateral elements are three and four, respectively; the sizes of tetrahedrons, triangular-prisms, pyramids, and brick elements are four, five, five, and six, respectively.

In the object space the element geometry is defined by $n_p$ interpolation (or control) points $\boldsymbol{r}_{[I]}$, where $[I] = [I_1, I_2, \ldots, I_\sigma]$ is a multi-index array of size $\sigma$, with integer entries $I_j \in [0, n_p]$ for $j = 1, \ldots, \sigma$. The element dependency relations further constrain the integer entries $I_j$ of the multi-index array, these constraints depending on the shape, size and dimension of the element [28]–[30]. The position vector in the object space is then expressed in terms of $n_p$ shape functions $P_{[I]}(\boldsymbol{\xi})$, usually of polynomial form, attached to each interpolation or control point

$$\boldsymbol{r}(\boldsymbol{\xi}) = \sum_{[I]} \boldsymbol{r}_{[I]} P_{[I]}(\boldsymbol{\xi}) \tag{2}$$

In the global object space, the element region is the entire set of points $\boldsymbol{r}(\boldsymbol{\xi})$ obtained by the mapping (2) of all the points of the parent region $E_\xi$ defined in (1).

## III. Singularity Cancellation in Parent Coordinates

Potential integrals on a given element are normally evaluated by subdividing the object-space element region into subdomains obtained by joining by a line each vertex of the entire domain to the given observation point $\boldsymbol{r}$ or, for 2D elements, to its projection onto the element or its extension [5], [11]. For 2D elements the subdomains are triangles whereas, in 3D, they are tetrahedrons or pyramids (see also [1]). This subdivision normally requires the re-parameterization of each subdomain with a sub-mapping of the kind given in (2).

Since the expansion functions are often given in terms of the parent coordinates of the entire element, while the potential integral kernels are expressed in terms of the global coordinates of the integration point, it is convenient to subdivide, whenever possible, the entire element directly in its parent space so to permit one to evaluate the kernel and the expansion functions using only one mapping. Direct subdivision is possible when the lines used to subdivide the object element are straight and are mapped, in the parent element, again by straight lines joining the parent vertices to a common point $\boldsymbol{\xi}^\circ$. This happens, for example, whenever the object element is defined by an *affine transformation* of the parent element. In the following, the object elements of this kind are called *hyper-straight*. For example, this is the case for rectilinear object-elements defined as in (2) by a mapping whose Jacobian is a non-zero constant (e.g., rectilinear triangles and tetrahedra, parallelograms, hexahedra with three pairs of parallel faces, etc.). In several applications, the majority of the elements are of the kind just described, although it is true that all the other cases have to deal with the more general, but more computationally intensive subdivision technique in the object space. Three fundamental properties are valid for hyper-straight elements: 1) the integration coordinates defined by our cancellation procedure define the parametric coordinates of all sub-elements via the same formula (see (3), (4), (38), (40) below); 2) the point about which the element is subdivided is the center of similarity transformations (see Section V and Appendix III); 3) the potential integrals on 3D hyper-straight elements are simplified by the application of these transformations.

A general procedure to subdivide an element directly in its parent space is presented in Appendix I. In the case of 2D elements, this procedure yields to the results of Section III-A. A discussion on application of this procedure to the case of 3D elements is deferred to Section V, with details reported in Appendix III.

In general, for a given element of size $\sigma$, a potential integral on $\boldsymbol{\xi}$ over the element region $E_\xi$ is subdivided into $\sigma$ sub-integrals, with integral subdomains obtained by joining a point $\boldsymbol{\xi}^\circ = (\xi_1^\circ, \xi_2^\circ, \ldots, \xi_\sigma^\circ)$ to each vertex of the parent domain (see Fig. 1). $\boldsymbol{\xi}^\circ$ is the arbitrarily located common origin of $\sigma$ different local pseudo-radial frames introduced to *locally* perform each sub-integral by properly changing the integration variables; the Jacobian of each variable transformation vanishes at $\boldsymbol{\xi}^\circ$.

In applications involving 3D elements, $\boldsymbol{\xi}^\circ$ is the parent point that maps the observation point $\boldsymbol{r}$ of the global object-space; notice that in the object space we use no superscript for the observation point $\boldsymbol{r}$, whereas the source (i.e., integration) point $\boldsymbol{r}'$ is primed. In applications involving planar 2D elements, $\boldsymbol{\xi}^\circ$ is the parent point that maps, in the global space, the normal projection $\boldsymbol{r}_p$ of the observation point $\boldsymbol{r}$ onto the element surface, or onto its planar extension. If the 2D element is non-planar, the 2D potential integrals are performed by working with a rectilinear planar patch of the object space that is tangent to the original curved one; in this case $\boldsymbol{\xi}^\circ$ is the point that maps the normal projection $\boldsymbol{r}_p$ of the observation point $\boldsymbol{r}$ onto this tangent patch.

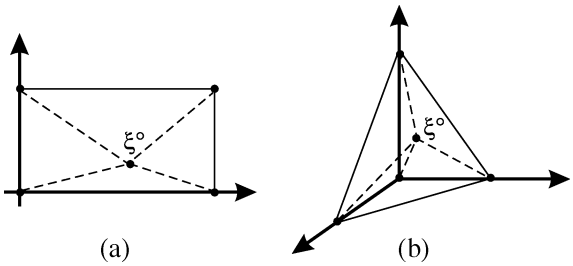



Fig. 1. A domain of size $\sigma$ is broken into $\sigma$ subdomains by joining the point $\boldsymbol{\xi}^\circ = (\xi_1^\circ, \xi_2^\circ, \ldots, \xi_\sigma^\circ)$ to each domain vertex. The figure illustrates the case for elements of size four: (a) the two-dimensional quadrilateral element is subdivided about the point $\boldsymbol{\xi}^\circ$ into four triangular subdomains; (b) the three-dimensional tetrahedral element is broken about the point $\boldsymbol{\xi}^\circ$ into four tetrahedral subdomains.

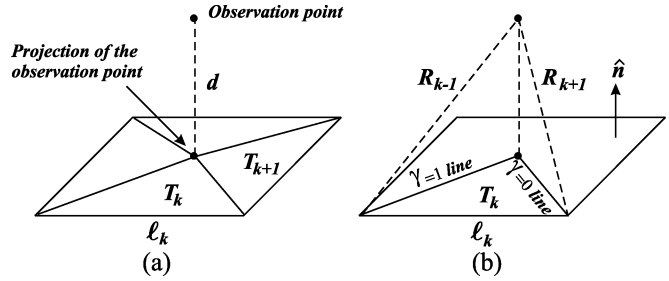



Fig. 2. A four-sided planar patch of the object space is broken into four triangular subdomains about the normal projection $\boldsymbol{r}_p$ of the observation point $\boldsymbol{r}$ onto the plane of the patch: (a) the distance from $\boldsymbol{r}$ to the plane of the patch is $d$; (b) $R_{k-1}$ and $R_{k+1}$ are the distances of the observation point from the two vertices of the $k$th side, whose length is $\ell_k$.

### A. Transformation Formulas for 2D Elements

When applied to 2D elements, the transformation formulas of Appendix I introduce a new pseudo-radial variable $\rho$, and a pseudo-angular variable $\Upsilon$. For 2D-elements, the pseudo-radial variable plays the same role as a radial variable of a cylindrical reference frame (centered at $\boldsymbol{\xi}^\circ$); for this reason, we call $\rho$ the pseudo-radial variable of 2D-elements, whereas we prefer to call $\nu$ the pseudo-radial variable of 3D elements. We now consider the parent triangular domain $T$, as well as the quadrilateral domain $Q$ shown in Fig. 1(a). As stated, these two domains are split into triangular subdomains with a common vertex at $\boldsymbol{\xi}^\circ$. Each subdomain retains only one edge of the original element, and $T_k$ indicates the sub-triangle that retains the $\xi_k = 0$ edge. Our procedure maps each subdomain $T_k$ into the square domain $\{\rho \in [0,1], \Upsilon \in [0,1]\}$.

The triangular domain $T$ is split into three subdomains $T_k$ ($k = 1, 2, 3$) with subscripts counted modulo three. For the $k$th subdomain, the variable transformation formulas (29) of Appendix I read as follows

$$\begin{cases} \xi_k = \xi_k^\circ(1-\rho) \\ \xi_{k+1} = \xi_{k+1}^\circ(1-\rho) + \rho\Upsilon \\ \xi_{k-1} = \xi_{k-1}^\circ(1-\rho) + \rho(1-\Upsilon) \end{cases} \tag{3}$$

with a Jacobian $\mathcal{J}_k = \xi_k^\circ \rho$. The above result is certainly not new. In fact, the current literature usually refers to the above transformation as the Duffy [4] or, sometimes, the Graglia transformation [5], [14], although the first user of this transformation is lost in the mists of time. In fact, for example, the same transformation was used in 1971 by Tracey [2], and by Stern and Becker in 1978 [3].

With reference to Appendix I, (3) is obtained by setting $\Upsilon_k = 0$ as per (31); the dependency relation (see [28]) $\Upsilon_k + \Upsilon_{k+1} + \Upsilon_{k-1} = 1$ then yields $\Upsilon_{k-1} = (1 - \Upsilon_{k+1})$. In this case, (3) is obtained from (29) by dropping the subscript in $\Upsilon_{k+1}$, that is by setting $\Upsilon = \Upsilon_{k+1}$.

For the quadrilateral domain $Q$, split into four subdomains $T_k$ ($k = 1, 2, 3, 4$), one counts the subscripts modulo four to write the two dependency relationships $(\xi_k + \xi_{k+2}) = 1$ and $(\xi_{k+1} + \xi_{k-1}) = 1$ (see [28]). For the $k$th triangular subdomain of $Q$, the variable transformation formulas (29) of Appendix I read as follows:

$$\begin{cases} \xi_k = \xi_k^\circ(1-\rho) \\ \xi_{k+2} = \xi_{k+2}^\circ(1-\rho) + \rho \\ \xi_{k+1} = \xi_{k+1}^\circ(1-\rho) + \rho\Upsilon \\ \xi_{k-1} = \xi_{k-1}^\circ(1-\rho) + \rho(1-\Upsilon) \end{cases} \tag{4}$$

with a Jacobian $\mathcal{J}_k = \xi_k^\circ \rho$. The coordinate lines $\Upsilon = 0$ and $\Upsilon = 1$ of the $k$th subdomain of a quadrilateral patch are shown in Fig. 2(b). With reference to Appendix I, (4) is obtained by setting $\Upsilon_k = 0$ as per (31); the dependency relationships then yield $\Upsilon_{k+2} = 1$ and $\Upsilon_{k-1} = (1 - \Upsilon_{k+1})$. Equations (4) are then obtained from (29) by simply dropping the subscript in $\Upsilon_{k+1}$.

Notice that (3) and (4) fully comply with the dependency relationships of the triangular and quadrilateral element, respectively. Both (3) and (4) can deal with a point $\boldsymbol{\xi}^\circ$ located outside the parent domain, or on its border. In fact, the integral on $T$ and $Q$ is the algebraic sum of the sub-integrals on the subdomains $T_k$ (for $k = 1, \ldots, \sigma$) where, for $\boldsymbol{\xi}^\circ$ located outside of the element, at least one of the parametric coordinates of $\boldsymbol{\xi}^\circ$ (say $\xi_i^\circ$) is negative, so that the corresponding Jacobian ($\mathcal{J}_i = \xi_i^\circ \rho$) is also negative whereas, for $\boldsymbol{\xi}^\circ$ lying on the border $\xi_j = 0$, the Jacobian $\mathcal{J}_j = \xi_j^\circ \rho$ vanishes together with the sub-integral on $T_j$.

## IV. Potential Integrals on 2D Elements

With reference to Fig. 2, let us consider a planar patch $S$ and a nearby observation point $\boldsymbol{r} = \boldsymbol{r}_p + d\hat{\boldsymbol{n}}$, where $\hat{\boldsymbol{n}}$ is the unit vector normal to $S$, $\boldsymbol{r}_p$ is the normal projection of $\boldsymbol{r}$ onto the plane of the patch, and $d$ vanishes whenever $\boldsymbol{r}$ lies on the patch-surface or its extension. The singularity cancellation procedure is applied to potential integrals of the form

$$\mathcal{I}_S = \int_S \boldsymbol{\Lambda}(\boldsymbol{r}') \frac{\exp(-jkR)}{4\pi R} \mathrm{d}S' \tag{5}$$

where $\boldsymbol{\Lambda}(\boldsymbol{r})$ is a vector or scalar basis function, $\boldsymbol{R} = \boldsymbol{r} - \boldsymbol{r}'$ is the vector distance from integration to observation point, and $R = |\boldsymbol{R}|$.

For each sub-triangle $T_k$, and in terms of the variables $(\rho, \Upsilon)$ defined in Section III-A, the distance from integration to observation point normalized with respect to the magnitude $\ell_k$ of the edge vector $\boldsymbol{\ell}_k$ reads as follows:

$$(\rho, \Upsilon) r = \frac{R(\rho, \Upsilon)}{\ell_k} = \sqrt{d_k^2 + \rho^2 \left(a_k^2 - b_k^2 \Upsilon + \Upsilon^2\right)} \tag{6}$$

where $d_k = d/\ell_k$ indicates the distance, normalized w.r.t. $\ell_k$, of the observation point from the plane of the patch, whereas $a_k$ and $b_k$ depend on the (unnormalized) distances $R_{k-1}$, $R_{k+1}$ of

the observation point from the two vertices of the sub-triangle $T_k$ opposite $\boldsymbol{r}_p$ [see Fig. 2(b)]

$$\begin{cases} a_k = r_{k+1} \\ b_k = \sqrt{1 + r_{k+1}^2 - r_{k-1}^2} \end{cases} \tag{7}$$

with

$$\begin{cases} r_{k-1} = \dfrac{\sqrt{R_{k-1}^2 - d^2}}{\ell_k} \\ r_{k+1} = \dfrac{\sqrt{R_{k+1}^2 - d^2}}{\ell_k} \end{cases} \tag{8}$$

and where $R_{k-1} = R(\rho = 1, \Upsilon = 1)$ and $R_{k+1} = R(\rho = 1, \Upsilon = 0)$. Notice that in Fig. 2(b) $\Upsilon$ increases clock-wise on the sub-triangle $T_k$ from $\Upsilon = 0$ to $\Upsilon = 1$, because of (3) and (4).

Successive variable transformations into parent (2) and then into pseudo-radial (3), (4) coordinates yield

$$\begin{aligned} \mathcal{I}_S &= \int_{E_\xi} \boldsymbol{\Lambda}(\boldsymbol{\xi}) \frac{\exp(-jkR)}{4\pi R} \mathcal{J} \mathrm{d}\boldsymbol{\xi} \\ &= \frac{\mathcal{J}}{4\pi} \sum_k \xi_k^\circ \int_0^1 \int_0^1 \boldsymbol{\Lambda}(\rho, \Upsilon) \exp(-jkR) \rho \frac{\mathrm{d}\Upsilon}{R} \mathrm{d}\rho \end{aligned} \tag{9}$$

where $\mathcal{J}$ is the Jacobian of the transformation (2) between global and parametric $\xi$-coordinates, and where it is henceforth understood that the distance $R$ from the observation to the integration point is expressed in terms of the integration variables in use (see for example (6)). The pseudo-radial transformation (3) or (4) produces a $\rho$ factor in the integrand that cancels out the singularity of (9) at $R = 0$ in the *non-displaced* case of $d = d_k = 0$. The modified Euler's substitution (see [31]) reported in Table I, first column, reduces (9) to

$$\mathcal{I}_S = \frac{\mathcal{J}}{4\pi} \sum_k \frac{\xi_k^\circ}{\ell_k} \int_0^1 \mathrm{d}\rho \int_0^1 \boldsymbol{\Lambda}(\rho, \varphi) \frac{\exp(-jkR)}{\varphi - \widetilde{\varphi}} \mathrm{d}\varphi \tag{10}$$

where $\varphi$ is the new integration variable replacing $\Upsilon$, and with

$$\widetilde{\varphi} = -C_k/\rho \tag{11}$$

As reported in Table I, $C_k$ is a real function of $\rho$ independent of $\varphi$, with $C_k > 0$ and $\widetilde{\varphi} < 0$ for all $\rho$ in the integration interval [0,1]. The integral (10) is evaluated numerically by integrating first along $\varphi$, that is for $\rho = const.$, and then on $\rho$. This integral simplifies considerably when the observation points lies on the patch-surface (self-element integration) or on its extension, that is for $d = 0$. In this case, the mapping reported at bottom of Table I yields a constant value for $C_k/\rho$ that does not depend on $\rho$

$$c_k = C_k/\rho = -\widetilde{\varphi} = \frac{r_{k-1} + r_{k+1} - 1}{2} > 0 \tag{12}$$

and the distance $R$ simplifies into the rational function (see Table I)

$$R = \ell_k \rho \left[ (\varphi - \widetilde{\varphi})(r_{k-1} + \widetilde{\varphi}) - \frac{\widetilde{\varphi}}{(\varphi - \widetilde{\varphi})} (1 - \widetilde{\varphi})(r_{k+1} + \widetilde{\varphi}) \right]. \tag{13}$$

It is interesting to observe that the static form of (10) in the case of a constant basis function $\boldsymbol{\Lambda}$ immediately yields

$$\mathcal{I}_S = \boldsymbol{\Lambda} \frac{\mathcal{J}}{4\pi} \sum_k \frac{\xi_k^\circ}{\ell_k} \int_0^1 \ln\left(1 + \frac{\rho}{C_k}\right) \mathrm{d}\rho \tag{14}$$

with

$$\mathcal{I}_S = \boldsymbol{\Lambda} \frac{\mathcal{J}}{4\pi} \sum_k \frac{\xi_k^\circ}{\ell_k} \ln\left(1 + \frac{1}{c_k}\right) \tag{15}$$

at $d = 0$. Thus, for $d = 0$, the free-space static potential of a constant source distribution is exactly integrated over a triangular and quadrilateral element by using only three ($k$ = 1,2,3) and four ($k = 1, \ldots, 4$) sampling points, respectively. The result (15) is equivalent to corresponding closed form results that can be obtained from several others published papers [1], [10]–[16], [19].

The pole in the kernel of (10) is easily cancelled by the transcendental transformation reported in the right-hand column of Table I, that yields

$$\mathcal{I}_S = \frac{\mathcal{J}}{4\pi} \sum_k \frac{\xi_k^\circ}{\ell_k} \int_0^1 \int_0^U \boldsymbol{\Lambda}(\rho, u) \exp(-jkR) \mathrm{d}u \mathrm{d}\rho \tag{16}$$

with

$$U = \ln\left[\frac{r(\rho, 0) + r(\rho, 1) + \rho}{r(\rho, 0) + r(\rho, 1) - \rho}\right] \tag{17}$$

in the general case of $d \neq 0$, and $U = \ln[(1 + c_k)/c_k]$ in the case $d = 0$. A variable transformation formula based on the use of the hyperbolic sine function to regularize (5) directly into an integral of the form of (16) has already been used in [1], thereby obtaining a result very similar to (16). Transcendental transformations of the same kind as [1] are also discussed in [8], [9].

Our Euler modified transformation permits one to *analytically* explain the reasons why numerical integration of near-singular integrals for small $d_k$ values is much more difficult than integration of the non-displaced singular integral, thereby showing, very clearly, the different degree of difficulty one has to deal with singular and near-singular displaced integrals. First of all, the pole of the kernel of (10) varies with $\rho$ in the near-singular *displaced* case, whereas $\widetilde{\varphi}$ is $\rho$-invariant in the singular $d_k = 0$ case. Secondly, after integration on $\varphi$, the remaining integral in $\rho$ always exhibits a kernel with a large dynamic range in the case of very small, non-vanishing $d_k$ values. This latter result is apparent if one considers the static logarithmic kernel of (14) and, in view of the integration by parts rule, it is intuitively expected to hold also for potentials associated with non-constant $\boldsymbol{\Lambda}$ functions. To further elaborate, the integral along $\varphi$ in

TABLE I
TWO SUCCESSIVE SUBSTITUTIONS FOR POTENTIAL INTEGRALS ON 2D ELEMENTS

| | Modified Euler's substitution to transform $\int \square \, \mathrm{d}\Upsilon \Longrightarrow \int \square \, \mathrm{d}\varphi$ | Final substitution to transform $\int \square \, \mathrm{d}\varphi \Longrightarrow \int \square \, \mathrm{d}u$ |
|---|---|---|
| Formulas for $d_k \neq 0$ | $\rho \dfrac{\mathrm{d}\Upsilon}{R} = \dfrac{1}{\ell_k} \dfrac{\rho \, \mathrm{d}\varphi}{(\varphi \rho + C_k)}$<br>$\Upsilon = \varphi \dfrac{\varphi(\rho + C_k) - (\varphi - 1) r(\rho, 0)}{\varphi \rho + C_k}$<br>$\varphi = \dfrac{\rho \Upsilon - r(\rho, 0) + r(\rho, \Upsilon)}{\rho - r(\rho, 0) + r(\rho, 1)}$ | $\dfrac{1}{\ell_k} \dfrac{\rho \, \mathrm{d}\varphi}{(\varphi \rho + C_k)} = \dfrac{1}{\ell_k} \mathrm{d}u$<br>$\varphi = \dfrac{C_k}{\rho} [\exp(u) - 1]$<br>$u = \ln\left(1 + \varphi \dfrac{\rho}{C_k}\right)$ |
| | with: $C_k = \dfrac{r(\rho, 0) + r(\rho, 1) - \rho}{2} > 0$ for $\rho \in [0, 1]$<br>$r(\rho, \Upsilon) = \dfrac{R(\rho, \Upsilon)}{\ell_k}$<br>Notice that at $\rho = 0$ one gets $\Upsilon = \varphi$, and $C_k(\rho = 0) = r(\rho = 0, \Upsilon) = d_k$. | |
| Simplified formulas for $d = d_k = 0$ | $\rho \dfrac{\mathrm{d}\Upsilon}{R} = \dfrac{1}{\ell_k} \dfrac{\mathrm{d}\varphi}{(\varphi + c_k)}$<br>$\Upsilon = \varphi \dfrac{(1 + c_k)\varphi - r_{k+1}(\varphi - 1)}{\varphi + c_k}$<br>$\varphi = \dfrac{\Upsilon - r_{k+1} + \sqrt{r_{k+1}^2 - (1 + r_{k+1}^2 - r_{k-1}^2)\Upsilon + \Upsilon^2}}{1 - r_{k+1} + r_{k-1}}$<br>with the very remarkable result:<br>$\dfrac{R}{\ell_k} = \rho \left[(\varphi + c_k)(r_{k-1} - c_k) + \dfrac{c_k (1 + c_k)(r_{k+1} - c_k)}{(\varphi + c_k)}\right]$ | $\dfrac{1}{\ell_k} \dfrac{\mathrm{d}\varphi}{(\varphi + c_k)} = \dfrac{1}{\ell_k} \mathrm{d}u$<br>$\varphi = c_k [\exp(u) - 1]$<br>$u = \ln\left(1 + \dfrac{\varphi}{c_k}\right)$ |
| | where $c_k = C_k/\rho = \dfrac{r_{k-1} + r_{k+1} - 1}{2} > 0$ | |

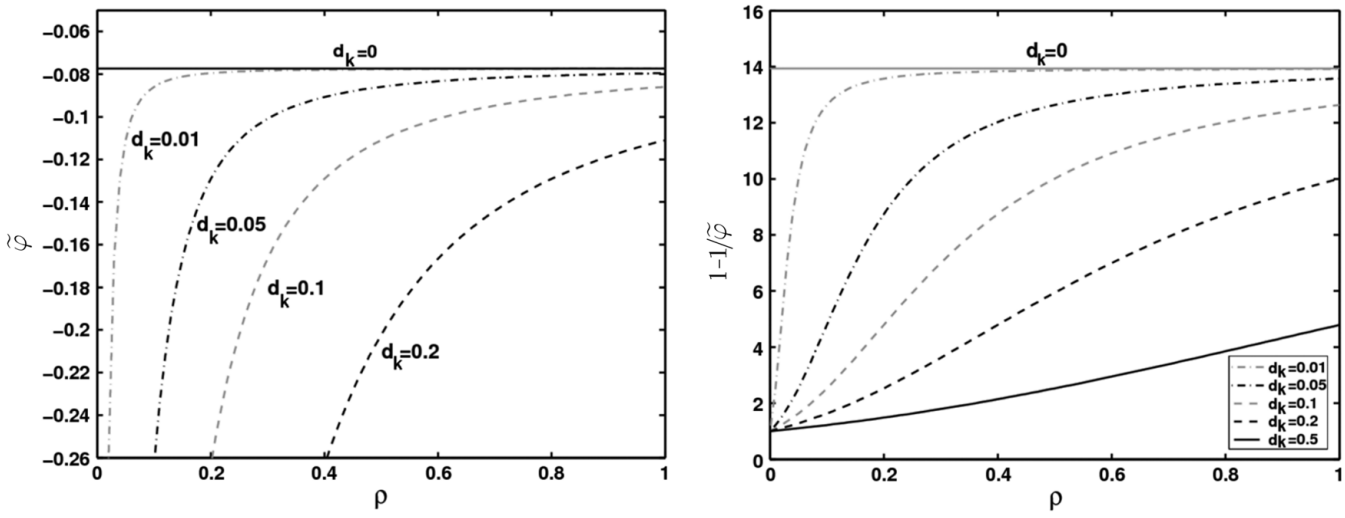



Fig. 3. Location in the $\rho$ axis of the pole $\widetilde{\varphi}$ (at left), and behavior of the argument $(1 - 1/\widetilde{\varphi})$ of the logarithmic kernel of (14) versus $\rho$ (at right), in the highly symmetrical case of an equilateral triangular domain with observation point at a normalized distance $d_k$ from its barycenter, $d_k$ being the ratio of the distance $d$ to the triangle side-length. The pole location and the kernel are $\rho$-invariant only for $d = 0$, where $\widetilde{\varphi}$ reaches its maximum value $\widetilde{\varphi}_{\max} = 1/2 - 1/\sqrt{3}$.

the displaced case is more difficult for $\rho \simeq 1$ because, for decreasing $\rho$ values, the pole $\widetilde{\varphi}$ is driven further away from the integration interval, as shown in (11). Conversely, $\widetilde{\varphi}$ is drawn near zero if $d_k$ decreases, since $C_k$ diminishes by decreasing $d_k$ (see, for example, Fig. 3 at left). The kernel of the integral in $\rho$ has a large dynamic range whenever $d_k$ is very small because of

the behavior of $\widetilde{\varphi}$; for example, in the highly symmetrical case considered in Fig. 3, the argument $(1-1/\widetilde{\varphi})$ of the logarithmic kernel of (14) changes rapidly whenever $0 < d_k \leq 0.1$, with a $\rho$-derivative that equals $1/d_k$ at $\rho = 0$. In the case of Fig. 3, for very small $d_k$, it is not hard to *predict* a logarithmic singularity at $\rho = \widetilde{\rho} \approx -d_k$, that is very close to the lower bound of the $\rho$ integration-domain. The knowledge of $\widetilde{\rho}$ could be used to perform more effectively the numerical integration in $\rho$ in the displaced case, although this extension goes beyond the scope of this paper. To our knowledge, this is the first time that it has been shown analytically that the displaced case of $d_k \neq 0$ is more difficult to handle numerically than the singular case.

Our modified Euler's transformation used to write (10) yields three very remarkable results. First of all it yields a regular integrand on the whole integration domain, provided $\boldsymbol{\Lambda}(\boldsymbol{\xi})$ is a regular function. Secondly, in cases where $\mathcal{J}\boldsymbol{\Lambda}(\boldsymbol{\xi})$ is a polynomial of the $\xi$ parent variables, this transformation converts $\mathcal{J}\boldsymbol{\Lambda}$ into a rational function of the $\varphi$ variable that has only one real-negative pole at $\varphi = \widetilde{\varphi}$ (i.e., outside of the integration domain), where $\widetilde{\varphi}$ is the same pole already present in the kernel of (10) (recall that (10) is integrated first in $\varphi$ and then in $\rho$, and that in the self-element case the pole location $\widetilde{\varphi} = -c_k$ is $\rho$-independent). Thirdly, one finds that even $R$ has only one simple pole, once again located at $\varphi = \widetilde{\varphi}$. In spite of the fact that the exponential factor $\exp(-jkR)$ exhibits an essential singularity at $\widetilde{\varphi}$, this singularity does not pose any numerical integration problem, as is quite evident for non-small values of $|\widetilde{\varphi}|$. A detailed discussion on the behavior of the exponential factor of (10) as a function of the new integration variables $(\rho, \varphi)$ is reported in Appendix II. More generally, for constant $\rho \in [0, 1]$, we proved using MATHEMATICA that the integral on the interval $\varphi = [0, 1]$ of the series (36) (given in Appendix II) converges very rapidly to the integral of $\exp(-jkR)/(\varphi - \widetilde{\varphi})$. That is to say that one can numerically evaluate (10) by use of a numerical quadrature scheme able to deal with functions that contain terms of the form $(\varphi - \widetilde{\varphi})^m$ and able to precisely consider, altogether, only the first few integer values of the exponent $m = 0, \pm 1, \pm 2, \ldots$, though we observe that there is no need to expand the integrand into series to integrate (10) numerically.

Effective Gauss-type quadrature rules that are exact for a mixture of polynomials and rational functions are available in the open literature, and a one-dimensional quadrature algorithm that fits the right-hand sides of (10) is the Gautschi algorithm 793 reported in [24]. Although we made no effort to specialize this algorithm to our case of a single real-negative pole, we deem this can be done, since this algorithm is quite general and able to deal with rather complex one-dimensional rational functions with multiple poles. The Gautschi algorithm is particularly suited for dealing with the non-displaced $d = 0$ case because of the constant value of $\widetilde{\varphi}$. It is also noteworthy that in the static limit $\exp(-jkR) = 1$ the entire integrand of (10) is a rational function of $\varphi$ whenever $\mathcal{J}\boldsymbol{\Lambda}(\boldsymbol{\xi})$ is a polynomial of the $\xi$ parent variables; in these particular cases, the singular and nearly singular static potentials are obtained *exactly* by using [24] to integrate on $\varphi$ and by Gauss-Legendre integration on $\rho$. The computational time to get the best result with [24] in the displaced $d \neq 0$ case is not optimum since the pole location $\widetilde{\varphi} = -C_k/\rho$ varies with $\rho$, so that to get *the best result* one has to re-evaluate the sample-points in $\varphi$, and their associated weights, whenever $\rho$ is changed. However, one can easily conceive several techniques to reduce the computational burden in the displaced case. For example, (10) can be evaluated by performing the integrals in $\varphi$ relative to two (or more) adjacent $\rho$-values $[\rho_i, \rho_{i+1}]$ by use of the same Gautschi's quadrature rule derived for the pole location $\widetilde{\varphi}_i$, or for an averaged pole location $\widetilde{\varphi}_{av} = (\widetilde{\varphi}_i + \widetilde{\varphi}_{i+1})/2$; the results obtained in this manner are usually much more accurate than those provided by Gauss-Legendre integration of (9).

To further appreciate the inherent superior accuracy of the results provided by (10) with use of Gauss-type quadrature rules of the kind given in [24] we recall that, for a constant $\rho \in [0, 1]$, as shown in (36) (Appendix II), the function $\exp(-jkR)/(\varphi - \widetilde{\varphi})$ is made of terms that can be integrated by the quadrature rules given in [24]. Then, with reference to (16), we further observe that, in spite of their simple expression, the functions $\boldsymbol{\Lambda}(\rho, u)$ and $R(\rho, u)$ appearing in the right-hand side of (16) are functions of the transcendental functions $\exp(\pm u)$, as noticed in [1]. Gauss-Legendre quadrature rules are readily available and have been used to compute the right-hand side of (16), usually obtaining accurate results [1]. However, in this connection, we point out that the functions $R$ and $\exp(-jkR)$ never take a polynomial form, whereas Gauss-Legendre quadrature works in a very *predictable* way and can be *exact* only when integrating polynomial functions. Moreover, in spite of the fact that in several applications $\mathcal{J}\boldsymbol{\Lambda}(\boldsymbol{\xi})$ has a polynomial expression in terms of the parent variable $\boldsymbol{\xi}$ (see [28]–[30]), the function $\boldsymbol{\Lambda}$ never takes a polynomial form in the $\rho - u$ domain, unless $\mathcal{J}\boldsymbol{\Lambda}(\boldsymbol{\xi})$ is constant. Therefore, some caution is required to numerically deal with (16), because the non-linear mapping used to obtain it could bring about further distortions whenever $\mathcal{J}\boldsymbol{\Lambda}(\boldsymbol{\xi})$ is a high-order polynomial of the parent variables $\boldsymbol{\xi}$, and this could be detrimental to numerical precision when using Gauss-Legendre quadrature.

For curved patches, the potentials are evaluated by applying the previous integration schemes on the rectilinear planar patch tangent to the original one, and that has the same shape (triangular or quadrilateral), the same element coordinates, Jacobian, edge vectors, and height vectors of the original curved patch at the point of tangency [28]. Although we do not consider these cases here, we remark that the number of quadrature points needed for a given accuracy is increased when dealing with curved patches with respect to the number required to deal with planar patches.

## V. Potential Integrals on 3D Elements

Our singularity cancellation procedure is now applied to potential integrals of the form

$$\mathcal{I}_V = \int_V \boldsymbol{\Lambda}(\boldsymbol{r}') \frac{\exp(-jkR)}{4\pi R} \mathrm{d}V' \tag{18}$$

where $V$ is the region of the entire 3D element. Table II summarizes the results obtained by subdividing the most common 3D-element geometries about the parent-point $\boldsymbol{\xi}^{\circ}$, according to the procedure described in Appendix I. As discussed in detail in

Appendix III, the integration is performed on volumetric subdomains via pseudo-radial coordinate transformations, thereby integrating first on layers parallel to the retained $\xi_k = 0$ face and then along the pseudo-radial $\nu$-direction. The variable transformations into parent and then into pseudo-radial coordinates yield

$$\mathcal{I}_V = \int_{E_\xi} \mathbf{\Lambda}(\boldsymbol{\xi}) \frac{\exp(-jkR)}{4\pi R} \mathcal{J} \mathrm{d}\boldsymbol{\xi} = \frac{\mathcal{J}}{4\pi} \sum_k \xi_k^\circ \sum_{ka} \frac{\zeta_{ka}}{\ell_{ka}} \mathcal{I}_{ka} \tag{19}$$

$$\mathcal{I}_{ka} = \int_0^1 \mathrm{d}\nu \int_0^1 \int_0^1 \mathbf{\Lambda}(\nu, \rho, \Upsilon) \exp(-jk\nu R_k) \nu\rho \frac{\mathrm{d}\Upsilon}{R_k/\ell_{ka}} \mathrm{d}\rho \tag{20}$$

where $\mathcal{J}$ is the Jacobian of the transformation (2) between global and parametric $\xi$-coordinates, and where the index $k$ of the outer summation considers all the element faces, while the index $ka$ of the inner summation considers all the edges of the $k$th face. In particular, with reference to Table II, the second dummy subscript $a$ of the index $ka$ is equal to $\ell$, $m$ or $n$ if face $k$ is triangular [see Appendix III, (38), (39)], or it is equal to $p$, $q$, $s$, $t$ when the $k$th face is quadrilateral [cf., Appendix III, (40), (41)]; the variable $\zeta_{ka}$ is the $a$th parent coordinate of the normal projection of the observation point $\boldsymbol{r}$ onto the $k$th element face. In the right-hand side of (20) we set $R = \nu R_k$, because of the dilation transformation (shown in Fig. 4) in which the distance $R$ from the observation point $\boldsymbol{r}$ to a given integration point $\boldsymbol{r}'(\nu, \rho, \Upsilon)$, located on the layer $\nu = const.$, is obtained by multiplying by $\nu$ the distance $R_k = |\boldsymbol{r} - \boldsymbol{r}'_k|$ from $\boldsymbol{r}$ to the point $\boldsymbol{r}'_k = \boldsymbol{r}'(\nu = 1, \rho, \Upsilon)$ that has the same $(\rho, \Upsilon)$ coordinates, but is located on the $k$th face. The Jacobian associated with the two pseudo-radial transformations contains a $\nu^2\rho$ factor; this serves to cancel out the singularity for $R = 0$, where $\nu$ and $\rho$ vanish. The modified Euler's transformation discussed in Section IV permits one to write (20) in the following form

$$\mathcal{I}_{ka} = \int_0^1 \nu \mathrm{d}\nu \int_0^1 \mathrm{d}\rho \int_0^1 \mathbf{\Lambda}(\nu, \rho, \varphi) \frac{\exp(-jk\nu R_k)}{\varphi - \widetilde{\varphi}} \mathrm{d}\varphi \tag{21}$$

with $\widetilde{\varphi} = -C_{ka}/\rho$. Notice here that $C_{ka}$ is evaluated once and for all by considering the $a$th triangular subdomain of the $k$th face, situated at a distance $d$ (i.e., at $\nu = 1$) from the observation point $\boldsymbol{r}$. The result for $C_k$ of Table I immediately yields

$$C_{ka} = \frac{r(\rho, 0) + r(\rho, 1) - \rho}{2} > 0 \tag{22}$$

where $r(\rho, 0)$ and $r(\rho, 1)$ are obtained by substituting into (6)–(8) $\ell_k$ with $\ell_{ka}$, and $d_k$ with $d/\ell_{ka}$. The transcendental transformation reported on the right-hand column of Table I finally yields

$$\mathcal{I}_{ka} = \int_0^1 \nu \mathrm{d}\nu \int_0^1 \int_0^U \mathbf{\Lambda}(\nu, \rho, u) \exp(-jk\nu R_k) \mathrm{d}\rho \mathrm{d}u \tag{23}$$

where the values of $U$ have already been discussed while presenting (17).

More work is required to assess the accuracy of the results obtainable by numerical integration of (20), (21) and (23) since the singularity of the integral kernel is cancelled out by the Jacobian factor $\nu^2\rho$, whereas a lower order factor of the form $\nu\rho$ would suffice. These studies will be considered in a future work. However, in this connection, we notice that the form of the Jacobian provided by our transformations permits one to deal with hypersingular potential integrals of the form

$$\int_V \mathbf{\Lambda}(\boldsymbol{r}') \boldsymbol{\nabla} \left[ \frac{\exp(-jkR)}{4\pi R} \right] \mathrm{d}V' \tag{24}$$

where $\boldsymbol{\nabla}$ operates on the unprimed object space coordinates, with

$$\boldsymbol{\nabla} \left[ \frac{\exp(-jkR)}{4\pi R} \right] = -\widehat{\boldsymbol{R}} \frac{\exp(-jkR)}{4\pi R^2} (1 + jkR) \tag{25}$$

and where $\widehat{\boldsymbol{R}}$ is the unit vector

$$\widehat{\boldsymbol{R}} = \frac{\boldsymbol{r} - \boldsymbol{r}'}{|\boldsymbol{r} - \boldsymbol{r}'|} \tag{26}$$

For the hypersingular part of (24), one gets

$$\int_V \widehat{\boldsymbol{R}} \mathbf{\Lambda}(\boldsymbol{r}') \frac{\exp(-jkR)}{4\pi R^2} \mathrm{d}V' = \frac{\mathcal{J}}{4\pi} \sum_k \xi_k^\circ \sum_{ka} \zeta_{ka} \mathcal{H}_{ka} \tag{27}$$

with

$$\mathcal{H}_{ka} = \int_0^1 \mathrm{d}\nu \int_0^1 \mathrm{d}\rho \int_0^1 \widehat{\boldsymbol{R}} \mathbf{\Lambda}(\nu, \rho, \Upsilon) \exp(-jk\nu R_k) \rho \frac{\mathrm{d}\Upsilon}{R_k^2} \tag{28}$$

and where two complex poles in the complex $\Upsilon$-plane are associated with the kernel denominator $R_k^2$ (for $\Upsilon$ real, $R_k$ does not vanish since $\xi_k^\circ \neq 0$ implies $d_k \neq 0$). The integral (28) can be numerically evaluated by direct use of the Gautschi algorithm without introducing any other variable transformation.

The procedure described in this Section for rectilinear elements can be extended to deal with potential integrals on curved three-dimensional elements. This extension will be considered in a future work.

## VI. Numerical Results

All the results of this Section were obtained by numerically integrating the potential (5) of a scalar function $\mathbf{\Lambda}(\boldsymbol{r})$ over a right triangle $T$ lying in the plane $z = 0$; the two perpendicular sides of $T$ lie on the positive $x$ and $y$ axes and are 1 [m] in length. By choosing the wavelength $\lambda = 2\pi/k$ in two different ways, $T$ defines two triangles of different size in wavelength. The first triangle $T_{10}$ is that of [1], [18], with $\lambda = 10$ [m] and vertices at $(0,0,0)(0.1\lambda,0,0),(0,0.1\lambda,0)$. The second triangle $T_1$ is obtained for $\lambda = 1$ [m], and it has a larger size in wavelength since its vertices are at $(0,0,0)(\lambda,0,0),(0,\lambda,0)$.

TABLE II
SUBDOMAINS AND PARENT-VARIABLE TRANSFORMATION FORMULAS FOR NON-DEGENERATE RECTILINEAR 3D ELEMENTS

**Transformation Formulas**

The most common 3D-element parent geometries of size $\sigma$ are subdivided about an arbitrarily chosen observation point $\boldsymbol{\xi}^\circ = (\xi_1^\circ, \xi_2^\circ, \ldots, \xi_\sigma^\circ)$ into $\sigma$ subdomains. The $k$-th subdomain (for $k = 1, \sigma$) is either a tetrahedron or a pyramid mapped by the $\Upsilon$-$\nu$ region $\nu \in [0,1]$, with all $\Upsilon$-variables in the interval $[0,1]$. For a given $k$-th subdomain, the formulas that map the $\nu$-$\Upsilon$ variables into the $\xi$ variables of the parent space are

$$\begin{cases} \xi_k &= \xi_k^\circ\,(1-\nu) \\ \xi_j &= \xi_j^\circ\,(1-\nu) + \nu \\ \xi_\eta &= \xi_\eta^\circ\,(1-\nu) + \nu\Upsilon_\eta \\ \text{with } \eta = \ell, m, n, p, q, s, \text{ or } t \end{cases} \qquad \text{with duplicated } \Upsilon\text{-dependency relations} \qquad \begin{cases} \Upsilon_\ell + \Upsilon_m + \Upsilon_n &= 1 \\ \Upsilon_p + \Upsilon_q &= 1 \\ \Upsilon_s + \Upsilon_t &= 1 \end{cases}$$

and transformation Jacobian $\mathcal{J}_k = \xi_k^\circ\,\nu^2$. In the rest of the Table, the $\Upsilon$-dependency relations are understood. The central column below reports the rules for the subscripts to obtain the $\xi$ parent variables appearing in the left-hand column.

| | Coordinate Dependency Relations | Subdomains | Measure of the Parent Cell |
|---|---|---|---|
| Tetrahedron [28] | $\xi_1 + \xi_2 + \xi_3 + \xi_4 = 1$<br><br>Independent coordinates: $\xi_1, \xi_2, \xi_3$ | for $k = 1, \ldots, 4$ (4 sub-tetrahedrons)<br>use $\xi_k$, $\xi_\ell$, $\xi_m$, $\xi_n$<br>with $\{\ell, m, n\} = \{k+1, k+2, k-1\}$<br>and subscripts counted modulo 4 | $\sum_{k=1}^{4} \int_{V_k} \mathrm{d}V_k = \sum_{k=1}^{4} \frac{\xi_k^\circ}{6} = \frac{1}{6}$ |
| Brick (see [28]) | $\xi_1 + \xi_4 = 1$<br>$\xi_2 + \xi_5 = 1$<br>$\xi_3 + \xi_6 = 1$<br><br>Independent coordinates: $\xi_1, \xi_2, \xi_3$ | for $k = 1, \ldots, 6$ (6 sub-pyramids)<br>use $\xi_k$, $\xi_j$, $\xi_p$, $\xi_q$, $\xi_s$, $\xi_t$<br>with $\{p, q\} = \{k+1, k+4\}$<br>$\{s, t\} = \{k+2, k+5\}$<br>$\{j\} = \{k+3\}$<br>and subscripts counted modulo 6 | $\sum_{k=1}^{6} \int_{V_k} \mathrm{d}V_k = \sum_{k=1}^{6} \frac{\xi_k^\circ}{3} = 1$ |
| Prism (see ref. [29]) | $\xi_1 + \xi_2 + \xi_3 = 1$<br>$\xi_4 + \xi_5 = 1$<br><br>Independent coordinates: $\xi_1, \xi_2, \xi_4$ | for $k = 1, 2, 3$ (3 sub-pyramids)<br>use $\xi_k$, $\xi_p$, $\xi_q$, $\xi_s$, $\xi_t$<br>with $\{p, q\} = \{k+1, k-1\}$<br>$\{s, t\} = \{4, 5\}$<br>and $p, q$ counted modulo 3<br><br>for $k = 4, 5$ (2 sub-tetrahedrons)<br>use $\xi_k$, $\xi_j$, $\xi_\ell$, $\xi_m$, $\xi_n$<br>with $\{\ell, m, n\} = \{1, 2, 3\}$<br>$\{j\} = \{9-k\}$ | $\sum_{k=1}^{5} \int_{V_k} \mathrm{d}V_k = \sum_{k=1}^{3} \frac{\xi_k^\circ}{3} + \sum_{k=4}^{5} \frac{\xi_k^\circ}{6} = \frac{1}{2}$ |
| Pyramid (see ref. [30]) | $\xi_1 + \xi_3 + \xi_5 = 1$<br>$\xi_2 + \xi_4 + \xi_5 = 1$<br><br>Independent coordinates: $\xi_1, \xi_2, \xi_5$ | for $k = 1, \ldots, 4$ (4 sub-tetrahedrons)<br>use $\xi_k$, $\xi_p$, $\xi_\ell$, $\xi_m$, $\xi_n$<br>with $\{\ell, m, n\} = \{k-1, k+1, 5\}$<br>$\{p, q\} = \{k+2, 5\}$<br>and subscripts counted modulo 4<br><br>for $k = 5$ (1 sub-pyramid)<br>use $\xi_k$, $\xi_p$, $\xi_q$, $\xi_s$, $\xi_t$<br>with $\{p, q, s, t\} = \{1, 3, 2, 4\}$ | $\sum_{k=1}^{5} \int_{V_k} \mathrm{d}V_k = \sum_{k=1}^{4} \frac{\xi_k^\circ}{6} + \frac{\xi_5^\circ}{3} = \frac{1}{3}$ |

The *reference* results of Table III used to evaluate the relative errors of the different integration techniques were obtained by iterative Gauss-Kronrod integration of (5) with the aid of the quadrature routine DTWODQ of the IMSL library. Though the numerical effort to obtain a reference result is irrelevant, we remark in passing that the computational time required to obtain each reference result is extremely high.

Integration of (5) via (9), (10) or (16) has been performed by subdividing the triangular domain into three triangles, according to the procedure explained in Section IV. Unlike the approach of [1], in the case of $d$ small but non-zero, the numerical integration has always been performed without any further subdivision of the radial integration domains. Therefore, in the following, the number of *radial samples* (or radial points) is the number of sampling points used for Gauss-Legendre integration along the radial $\rho$-direction, which is performed according to the quadrature formulas of [32], whereas the number of *transverse samples* is the number of sampling points used to integrate along the $\varphi$, $\Upsilon$ or $u$ direction. Since we integrate numerically over 3 sub-triangles, the total number of sampling points is equal to 3 $\times$ the number of radial samples $\times$ the number of transverse samples.

All integrals have been evaluated numerically in double precision (Intel Pentium-M Centrino, 1.4 GHz, 512 MB RAM). To account for possible uncertainties in the reference solution and the incidental presence of error propagation effects, we cautiously assume a result to be *numerically exact* if its relative

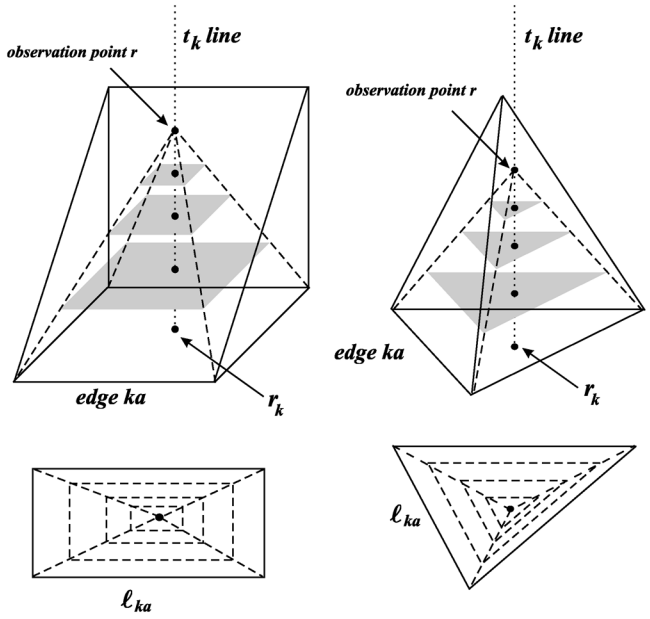



Fig. 4. An element is subdivided about the observation point $\boldsymbol{r}$ into subdomains. The $k$th subdomain of the prism (top-left) and of the tetrahedron (top-right) is backed up by the $k$th face of the element. $\ell_{ka}$ is the length of the edge $ka$ common to face $k$ and $a$; $\boldsymbol{r}_k$ is the normal projection of $\boldsymbol{r}$ onto the $k$th face of the element. In the subdomain bottom-views shown at bottom, the normal projections of $\boldsymbol{r}$ on all the layers parallel to the $k$th face collapse into the same point.

error is lower than $10^{-13}$ with respect to the result of Table III. Hence, the figures of this Section report the number of significant digits of the numerical results, with the $10^{-13}$ error level simply represented by a straight-line, which we call the *floating error level* line. In all the figures of this Section, the results obtained using the Gautschi algorithm to integrate (10) are marked by stars, while the circle-results are obtained using the integration technique presented in [1]. The circle-results always coincide with the results obtained by Gauss-Legendre integration of (16); these latter are marked by dots whenever reported.

We first consider results for the static case, $k = 0$. In case of polynomial $\boldsymbol{\Lambda}(\boldsymbol{\xi})$ functions, Gautschi's integration of the static form of (10) yields machine precision results by using radial and transverse samples in the number given in Table IV. In fact, the most important feature of the Gautschi integration scheme is its ability to *exactly* integrate, for $d = 0$, the static potential of any polynomial source distribution of order $n$ using only $n_0 = n+1$ transverse samples and $m_0 = \lceil (n+1)/2 \rceil$ radial samples, $m_0$ being the smallest integer greater than or equal to $(n+1)/2$. This unique property is due to the following facts: 1) in the static case and for $d = 0$, the integrand of (10) is a rational function of $\varphi$ and a polynomial function of $\rho$; 2) the numerical integration in $\varphi$ is performed using Gautschi's generalized Gaussian quadrature, while integration in $\rho$ is done using standard Gauss-Legendre quadrature. A higher number of $\rho$-samples is needed for $d \neq 0$, where the integrand of (10) is no longer a polynomial function of $\rho$ because of the $\rho$-dependence of the pole $\widetilde{\varphi}$. However, at $\rho = const.$, the integrand is still a rational function of $\varphi$, so that the number of the transverse samples required for the exact Gautschi's integration remains the same as for $d = 0$. The number of samples reported in Table IV to deal with different $d$ values is validated for functions of order $n \leq 5$ (basis functions of order less than five are normally used in applications). In the case of small, non-vanishing $d$ values, the number of radial samples has to be chosen within a range as specified in Table IV. This happens for normalized distances $d/\ell_{\max} < 1$, where $\ell_{\max}$ is the length of the largest side of the integration domain in the global reference-frame. The upper value of the range should be used to deal with observation points located in the neighborhood of a vertex of the integration domain (worst cases); the number of the radial samples can be reduced whenever the normal projection of the observation point on the plane of the source domain is not close to a vertex. The data of Table IV are more than safe; in fact, there are many cases where machine precision results can be obtained with a lower number of radial samples.

As stated, the static case of a constant source distribution is too simple to make any numerical comparison, and in Fig. 5 we consider the static potential of the quartic source distribution $\boldsymbol{\Lambda}(\boldsymbol{r}) = x_T^4$ over the triangle $T$, with observation point $(x, y, z) = (0.1, 0.1, d)$ [m], for $d = 0$ (Fig. 5, at left) and $d = 0.01$ [m] (at right). Fig. 5 shows that the circle and dot results always coincide. Above all, in agreement with Table IV, this figure shows that Gautschi's integration with 5 transverse samples yields the exact result with 3 and 64 radial samples at $d = 0$ and $d = 0.01$ [m], respectively. Notice in fact that the numerical precision of the Gautschi results increases abruptly by eleven significant figures when going from 4 to 5 transverse samples for the appropriate number of radial samples; whereas Gauss-Legendre integration of (16) with 5 transverse samples looses at least 10 significant figures with respect to the exact result.

We now discuss numerical results for the dynamic case, where the integrands of (5) and (10) contain the extra factor $\exp(-jkR)$. To appropriately deal with this *modulation* factor, the number of integration samples must increase with respect to the static case by a number that depends on the size in wavelengths $\ell_{k\max}/\lambda$ of the triangular integration-subdomains, where $\ell_{k\max}$ is the length of the largest side of the triangular integration subdomains in the global reference-frame. The additional number of samples needed to integrate (10) is reported in Table V; these results hold for any value of the distance $d$. Notice however that the effect of the exponential factor on the number of radial samples is usually less important in the displaced cases of $0 < d/\ell_{\max} \leq 0.1$, since these cases already require a higher number of radial samples because of Table IV. The data of Table V are safe; once again, there are many dynamic cases where machine precision results can be obtained with a smaller number of samples than that given in Tables IV and V.

Fig. 6 shows the results of (5) for an observation point $(x, y, z) = (0.1, 0.1, 0)$ [m] in the case of a constant source distribution over the triangle $T_{10}$ where, with reference to Table V, one has $\ell_{k\max}/\lambda = \sqrt{2}/10 \approx 0.14$. The left-hand side of Fig. 6 and Table V show that machine precision results can be obtained by using at least five radial samples. In fact, for a fixed number of radial samples, the precision of the results remains constant with respect to the number of the transverse samples after this number crosses a certain threshold value. Saturation is reached below the floating error level when the

TABLE III
REFERENCE VALUES FOR SINGULAR AND DISPLACED ($d \neq 0$) NEAR-SINGULAR POTENTIAL INTEGRALS OVER THE SOURCE TRIANGLE $T$

| | $\boldsymbol{\Lambda}(\boldsymbol{r})$ | Observation Point [m] | | $4\pi\mathcal{I}_S = \int_S \boldsymbol{\Lambda}(\boldsymbol{r}') \frac{\exp(-j2\pi R/\lambda)}{R} \mathrm{d}S'$ | | See Fig. # |
|---|---|---|---|---|---|---|
| | | $x = y$ | $z = d$ | Real | Imaginary | |
| $\lambda = \infty$ | 1 | $x_o$ | 0.0 | 1.90214591770239 | 0.0 | |
| | | | 0.01 | 1.84529014784452 | 0.0 | |
| | | | 0.10 | 1.52367523037142 | 0.0 | |
| | $x_T^4$ | $x_o$ | 0.0 | 0.107131914758450 | 0.0 | |
| | | | 0.01 | 0.103951219990467 | 0.0 | |
| | | | 0.10 | 0.0877623939045149 | 0.0 | |
| | 1 | 0.1 | 0.01 | 1.87918375312867 | 0.0 | |
| | $x_T^4$ | 0.1 | 0.0 | 0.0562390551783612 | 0.0 | 5 |
| | | | 0.01 | 0.0562210406396374 | 0.0 | 5 |
| $\lambda = 10$ [m] | 1 | $x_o$ | 0.0 | 1.86562247517596 | −0.310885377661594 | 8 |
| | | 0.1 | 0.0 | 1.89857266176847 | −0.309643085636859 | 6,9 |
| | | | 0.01 | 1.83755816482971 | −0.309641036420311 | |
| | | | 0.10 | 1.42970516324654 | −0.309438204123196 | 10 |
| | $x_T \times y_T \times w_T$ | 0.1 | 0.0 | 0.0280347391474516 | −0.00517689166514125 | 9 |
| | $x_T^4$, or $y_T^4$ | 0.1 | 0.0 | 0.0521367500013373 | −0.0203707188804882 | 9 |
| | | | 0.01 | 0.0521182008520720 | −0.0203705833443571 | 11 |
| | | | 0.10 | 0.0509722079057609 | −0.0203571679283724 | |
| | $w_T^4$ | 0.1 | 0.01 | 0.354339361066546 | −0.0208966653996137 | 11 |
| $\lambda = 1$ [m] | 1 | $x_o$ | 0.0 | −0.0296130847106268 | −1.00395495969246 | 9 |
| | $x_T \times y_T \times w_T$ | $x_o$ | 0.0 | 0.000740171902685337 | −0.0240661287189359 | 9 |
| | $x_T^4$, or $y_T^4$ | $x_o$ | 0.0 | −0.0165473311076690 | −0.0391294772307506 | 9 |
| | $w_T^4$ | 0.1 | 0.0 | 0.379185916579646 | −0.0208968030187709 | |
| | $x_T^9$ | $x_o$ | 0.0 | −0.0124027954233261 | 0.00130288604501147 | |

where $w_T = 1 - x_T - y_T$, and $x_o = 0.488217389773805$

TABLE IV
NUMBER OF INTEGRATION POINTS FOR MACHINE PRECISION EVALUATION OF THE STATIC ($k = 0$) POTENTIAL OF POLYNOMIAL SOURCES OF THE PARENT VARIABLES

| Normalized distance $d/\ell_{\max}$ | Polynomial order of the source term $\mathcal{J}\,\boldsymbol{\Lambda}(\boldsymbol{\xi})$ | Number of samples for Gautschi integration of (10) | | Order of Dunavant formula |
|---|---|---|---|---|
| | | radial | transverse | |
| 0.0 | $n = 0$ | use eq. (15) | use (15) | — |
| | $n \geq 1$ | $m_0 = \left\lceil \frac{n+1}{2} \right\rceil$ | $n_0 = n + 1$ | |
| 0.005 | $n \leq 5$ | $80 \div 104$ | $\max\{2, n_0\}$ | — |
| 0.01 | $n \leq 5$ | $64 \div 80$ | $\max\{2, n_0\}$ | — |
| 0.05 | $n \leq 5$ | $24 \div 48$ | $\max\{2, n_0\}$ | — |
| 0.1 | $n \leq 5$ | $20 \div 32$ | $\max\{2, n_0\}$ | — |
| 0.5 | $n \leq 5$ | $10 \div 16$ | $\max\{2, n_0\}$ | — |
| 1 | $n \leq 5$ | $m_0 + 7$ | $\max\{2, n_0\}$ | $n + 17$ |
| 10 | $n \leq 5$ | $m_0 + 3$ | $m_0 + 2$ | $n + 6$ |
| 100 | $n \leq 5$ | $m_0 + 2$ | $m_0 + 2$ | $n + 4$ |
| 500 | $n \leq 5$ | $m_0 + 1$ | $m_0 + 1$ | $n + 2$ |
| $10^3$ | $n \leq 5$ | $m_0 + 1$ | $m_0 + 1$ | $n + 2$ |
| $10^5 \div 10^6$ | $n \leq 5$ | $m_0$ | $\max\{2, m_0\}$ | $n$ |

$d/\ell_{\max}$ is the distance from the observation point to the plane of the integration domain, normalized w.r.t. $\ell_{\max}$ (the length of the largest side of the integration domain in the global reference-frame);

$m_0$ is the smallest integer greater than or equal to $(n + 1)/2$.

Whenever the static ($k = 0$) potential (5) of the polynomial source distribution $\boldsymbol{\Lambda}(\boldsymbol{\xi})$ is computable to machine precision by Gauss quadrature, the right-hand column reports the order of the Dunavant rule that can be used (see [33]).

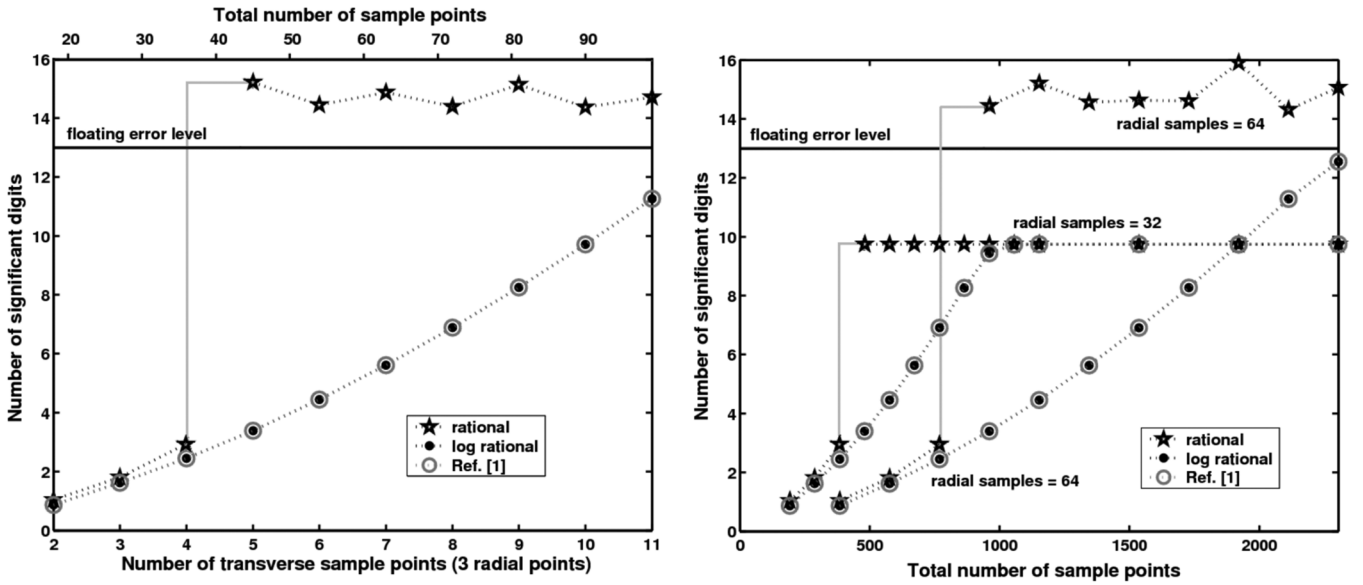



Fig. 5. Convergence comparison for the static potential of the source distribution $\mathbf{\Lambda}(\mathbf{r}) = x_T^4$ over the right-triangle $T$, with observation point $(x, y, z) = (0.1, 0.1, d)$ [m]. The results for $d = 0$ (at left) and for $d = 0.01$ [m] (at right) prove that convergence with 5 transverse samples is assured only by Gautschi's integration of (10); this further guarantees machine precision results with 3 and 64 radial samples in the case of $d = 0$ and $d = 0.01$ [m], respectively.

TABLE V
ADDITIONAL NUMBER OF SAMPLES FOR MACHINE PRECISION EVALUATION OF THE DYNAMIC POTENTIAL OF POLYNOMIAL SOURCES OF THE PARENT VARIABLES

| Size of the triangular integration-subdomain in wavelengths | Additional number of samples for Gautschi integration of (10) | |
|---|---|---|
| | radial | transverse |
| $1/2 < \ell_{k\max}/\lambda \leq 1$ | $\Delta_m = 8$ | $\Delta_n = 15$ |
| $1/3 < \ell_{k\max}/\lambda \leq 1/2$ | $\Delta_m = 6$ | $\Delta_n = 11$ |
| $10^{-1} < \ell_{k\max}/\lambda \leq 1/3$ | $\Delta_m = 5$ | $\Delta_n = 9$ |
| $2 \times 10^{-2} < \ell_{k\max}/\lambda \leq 10^{-1}$ | $\Delta_m = 4$ | $\Delta_n = 7$ |
| $10^{-2} < \ell_{k\max}/\lambda \leq 2 \times 10^{-2}$ | $\Delta_m = 3$ | $\Delta_n = 5$ |
| $10^{-3} < \ell_{k\max}/\lambda \leq 10^{-2}$ | $\Delta_m = 2$ | $\Delta_n = 3$ |
| $10^{-6} < \ell_{k\max}/\lambda \leq 10^{-3}$ | $\Delta_m = 1$ | $\Delta_n = 2$ |
| $0 < \ell_{k\max}/\lambda \leq 10^{-6}$ | $\Delta_m = 1$ | $\Delta_n = 1$ |
| $\ell_{k\max}$ is the length of the largest side of the triangular integration subdomain(s) in the global reference-frame. Notice that $\Delta_n \simeq 2\Delta_m$. | | |

number of radial samples is equal or lower than four, whereas one can attain the floating error level with five or more radial samples. In Fig. 6, the threshold values in the number of transverse samples for the star (or the circle) results are 4 (4), 6 (7), and 7 (10) for 2, 3 and 4 radial samples, respectively. Use of the Gautschi algorithm to integrate (10) improves the convergence of the numerical results to the exact value, with respect to the convergence obtained by Gauss-Legendre integration of (16). To obtain results to machine precision with 5 radial samples, the Gautschi algorithm requires 8 transverse samples whereas Gauss-Legendre integration of (16) requires 11 transverse samples (for this case, Tables IV and V predict $1 + 9 = 10$ transverse samples). Notice also how, for a fixed number of total samples, Gautschi integration of (10) increases by one to three the number of significant figures of the result with respect to the number of significant digits obtained by Gauss-Legendre integration of (16). For example, Fig. 6 at left shows that with 7 transverse and 5 radial samples the star result is correct to 12 significant figures whereas, for the circle result, one counts 9 significant figures.

The computational time to evaluate (5) via Gauss-Legendre integration of (16) is of the order of $10^{-4}$ seconds which, at present, is 10 to 20 times less than the time required to evaluate (5) via Gautschi integration of (10), to achieve the same machine precision. In this connection, we recall that the precision of Gauss-Legendre integration of (16) is hardly predictable. There are two reasons for this difference in the computational times. First of all, Gauss-Legendre integration is done by use of pre-tabulated weights and samples, whereas the weights and the samples used for Gautschi integration are always computed by use of the robust, general purpose routines available in [24]. Secondly, the routines in [24] are not specialized to deal with integrals of the form of (5); in fact, these routines are intended to deal with multiple complex poles of the integrand, whereas the kernel of (10) has only one real-negative pole at $\varphi = \widetilde{\varphi}$. Finally we remark that, in practice, the computation time required to evaluate (5) via Gautschi integration of (10) usually diminishes by increasing the number of the transverse samples, with a speed-up factor in the range from 2 to 5. This apparently counter-intuitive effect occurs because the Gautschi algorithm finds the integration and weighting points by first solving an eigenvalue problem, which becomes better conditioned when the number of sampling points is increased. Thus although Gauss-Legendre integration of (16) is much faster than Gautschi integration of (10) if the number of the transverse samples is small, it is often convenient to over-sample in the transverse direction while using the Gautschi algorithm, so to reduce the computational burden and, at the same time, to obtain the desired numerical precision.

We consider the case-study of Fig. 6 because it was previously considered in [1] and [18]. However, in most moment method

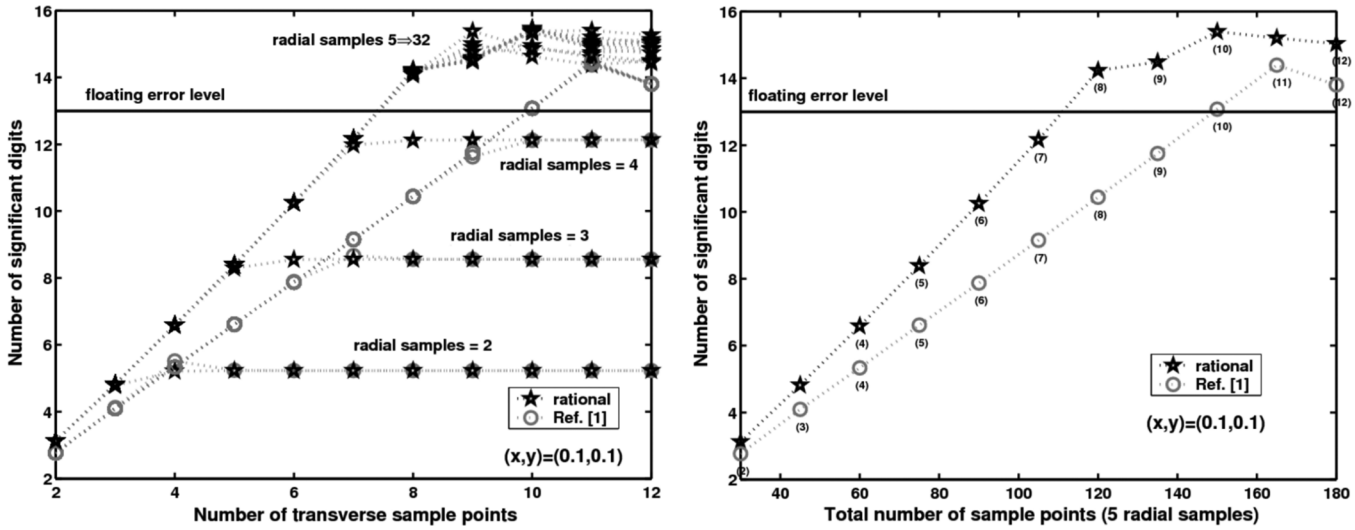



Fig. 6. Convergence comparison for self-term integration over $T_{10}$, with observation point $(x, y, z) = (0.01\lambda, 0.01\lambda, 0)$ and $\mathbf{\Lambda}(\boldsymbol{r}) = 1$. The results at left are for a number of radial points that goes from 2 to 32. The results obtained with 5 radial points are given at right by reporting in parenthesis the number of transverse samples used.

applications, the observation point of the potential integral is actually chosen by the quadrature scheme that performs the *testing* integral. The testing integral is non-singular and is usually evaluated by Gaussian quadrature. For example, very efficient quadrature rules for the triangle are given in [33], and there would really be no reason to evaluate potential integrals to machine precision to loose all the precision while performing the second testing integral. It is therefore convenient to assess the convergence properties of the numerical schemes to integrate (5) with respect to the observation points that are the quadrature points of the (second) testing integral. Critical situations occur whenever the observation point is very close to one of the integration domain edges. A parameter that is able to properly quantify critical situations in the non-displaced case of $d = 0$ is the value of the constant $c_k$ given in (12). For very small values of $c_k$, the upper bound $U$ of the integral in $u$ on the right-hand side of (16) tends to be rather high, since one has $U \approx 2.3q$ for $c_k \approx 10^{-q}$ and $q \geq 3$, whereas the pole at $\widetilde{\varphi} = -c_k$ of the kernel on the right-hand side of (10) tends to be very close to the lower integration bound $\varphi = 0$. Notice however that a zero value of $c_k$ is not at all critical since, in this case, the area of the subtriangle associated with this $c_k$ vanishes together with $\xi_k^\circ$ in (10) and (16); as a matter of fact, one can usually neglect the integral contribution of subtriangles whose $c_k$ and $\xi_k^\circ$ values are smaller than $10^{-6}$. As previously stated, the integration domain of (5) is subdivided into subtriangles about the given observation point, and each subtriangle has its own $c_k$ value; therefore, we quantify critical situations by using the minimum of these values. High values of minimum $c_k$ correspond to non-critical situations, whereas (5) becomes critical whenever the minimum $c_k$ is too small. For example, the case of Fig. 6 is considered to be non-critical since the minimum of the three values of $c_k$ is equal to $2.3 \times 10^{-2}$ (with a corresponding $U_{\max} \approx 3.8$). It is of importance to observe that $c_k$ in (12) does not depend on the wavelength and is expressed in terms of normalized distances, so that the $c_k$ values are influenced only by the element shape in the global object space and not by the element width. Fig. 7, for example, reports the contour plot of the minimum value of the constants $c_k$ as a function of the parent observation point coordinates $(\xi_1, \xi_2, \xi_3 = 1 - \xi_1 - \xi_2)$ of the triangular simplex (at left), and as a function of the parent observation point coordinates $(\xi_1, \xi_2, \xi_3 = 1-\xi_1, \xi_4 = 1-\xi_2)$ of the parent quadrilateral element (at right). For the sake of clarity, Fig. 7 considers only the case of observation points located in the element internal region (self-element case), although critical situations for $d = 0$ occur also in case of observation points located outside of the element region, whenever the observation point is very close to one side of the entire element. Numerical integration of (5) over object space elements having the shape of those of Fig. 7 is critical if the observation point happens to be located in the *darker regions* of the figure, where the minimum $c_k$ is very small. The choice of the quadrature rule to evaluate the moment method testing integrals over elements of this kind should then be made so as to reduce, if possible, the number of quadrature points in the darker regions of Fig. 7.

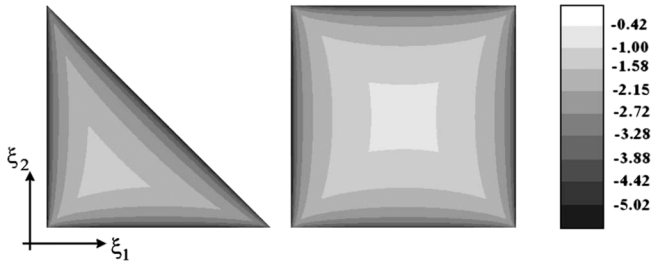



Fig. 7. Contour plot of the logarithm to base 10 of the minimum value of the constants $c_k$ for the triangular simplex $E_\xi = \{\xi_i | \xi_i \geq 0, \forall i \in [1, 3]\}$, at left, and for the parent quadrilateral element $E_\xi = \{\xi_i | \xi_i \geq 0, \forall i \in [1, 4]\}$, at right. The markers of the greyscale bar are at $-0.42$ (i.e., $c_k = 0.3802$), $-1.00$ ($c_k = 0.1$), $-1.58$ ($c_k = 0.0263$), etc. Numerical integration of (5) in the non-displaced case of $d = 0$ becomes critical whenever the observation point is very close to one edge of the integration domain, that is in the darker regions of the elements shown.

The results reported in Fig. 8 consider a typical critical situation and are again relative to a self-element case for the triangle $T_{10}$, with $\mathbf{\Lambda}(\boldsymbol{r}) = 1$. With respect to Fig. 6 we have only

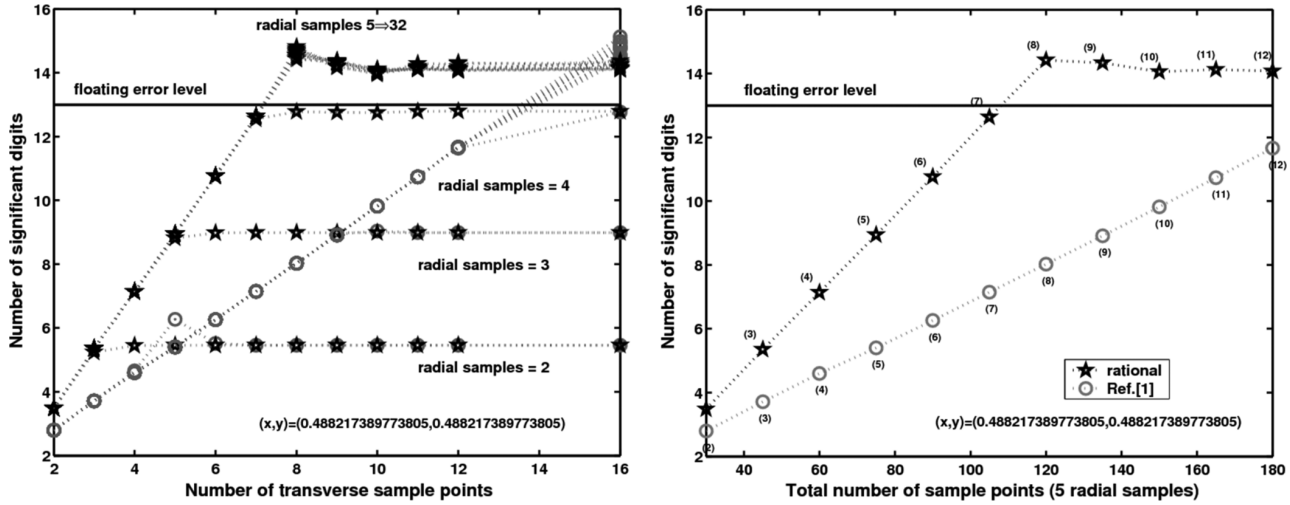



Fig. 8. Convergence comparison for self-term integration over $T_{10}$ with $\mathbf{\Lambda}(\boldsymbol{r}) = 1$, in the critical situation of minimum $c_k$ approximately equal to $1.39 \times 10^{-4}$. The global coordinates $(x, y)$ of the observation point are reported in meters in the body of the figure. The results at left are for a number of radial points that goes from 2 to 32. Results obtained with 5 radial samples are given at right by reporting in parenthesis the number of transverse points used.

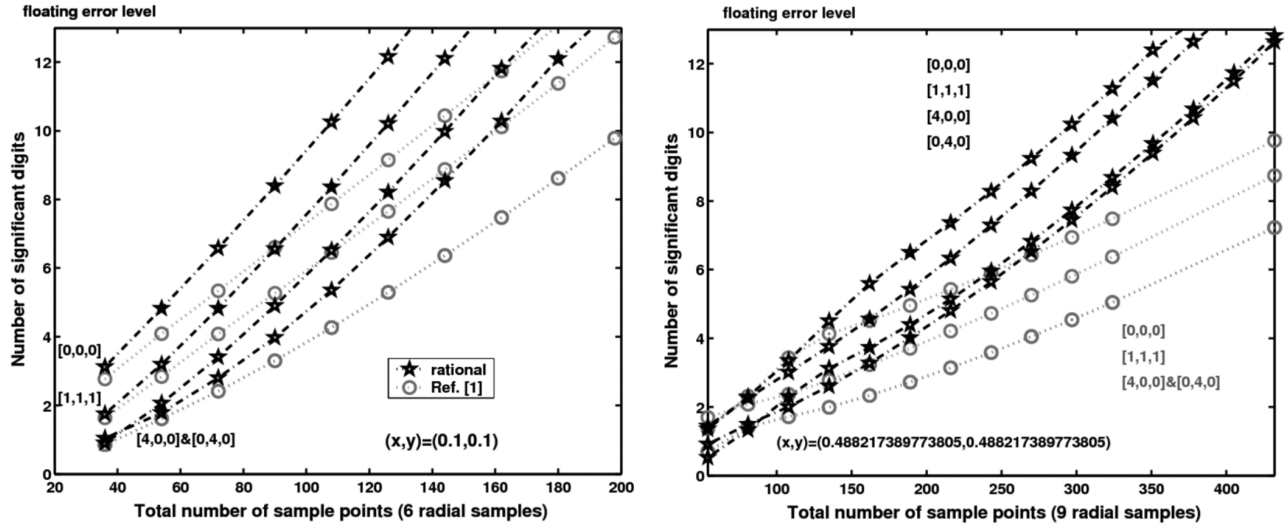



Fig. 9. Convergence comparison for self-term integration over $T$ at different wavelengths and observation points, in case of $\mathbf{\Lambda}(\boldsymbol{r}) = x_T^a y_T^b (1 - x_T - y_T)^c$. In the body of the figure, the exponents $[a, b, c]$ of the function $\mathbf{\Lambda}(\boldsymbol{r})$ label the results, and the global coordinates $(x, y)$ of the observation point are reported in meters. The results relative to integration over $T_{10}$, with $\lambda = 10$ [m] are given at left; the results relative to integration over $T_1$, with $\lambda = 1$ [m], are reported at right.

changed the position of the observation point, whose global coordinates $(x, y)$ are reported in meters in the body of the figure (notice that $x = y$). This observation point has been chosen from the 33 points that are used for a symmetrical Gaussian quadrature over the triangle $T$, according to the quadrature rule of degree 12 given in [33]. The observation point at issue here is that associated with the minimum value of $c_k \approx 1.39\ 10^{-4}$, with $\log_{10}(c_k) = -3.857$ and $U_{\max} \approx 8.88$. In this case, the improvement in convergence of the results toward the exact solution provided by Gautschi's integration of (10) is more evident than that shown in Fig. 6. In fact, to obtain results to machine precision with 5 radial samples, the Gautschi algorithm still requires 8 transverse samples whereas Gauss-Legendre integration of (16) now requires more than 12 transverse samples. Notice also how, for a fixed number of total samples, Gautschi integration of (10) now increases by one to five the number of significant figures of the result with respect to the number of significant digits obtained by Gauss-Legendre integration of (16). For example, Fig. 8 at left shows that with 7 transverse and 5 radial samples the star result is correct to more than 12 significant figures whereas, for the circle result, one counts 7 significant figures.

The results for the integral (5) reported on the left-hand side of Fig. 9 are relative to triangle $T_{10}$ in the self-element case already considered in Fig. 6, whereas the results on the right-hand side are relative to triangle $T_1$ in the self-element critical case of observation point located as in Fig. 8. The global coordinates $(x, y)$ of the observation point are reported in meters in the body of the figure, which consider four different polynomial $\mathbf{\Lambda}$ functions. The exponents $[a, b, c] (= [0, 0, 0], [1, 1, 1], [4, 0, 0], [0, 0, 4])$ of the scalar function $\mathbf{\Lambda}(\boldsymbol{r}) = x_T^a y_T^b (1 - x_T - y_T)^c$ label the results in the figure. Notice how Gauss-Legendre integration of (16) for $\mathbf{\Lambda}(\boldsymbol{r}) = x_T^4$ and $\mathbf{\Lambda}(\boldsymbol{r}) = y_T^4$ gives results of the same precision, although there are differences in the numerical values of these results (the numerical precision obtained by Gauss-Legendre integration of (16) does not permit showing in the figure the differences between the two results). The quality of the results obtained

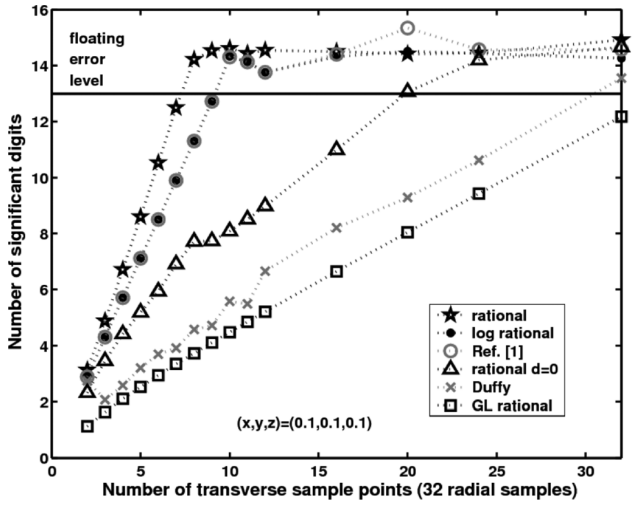



Fig. 10. Convergence comparison for a nearly singular integral over $T_{10}$, with observation point $(x, y, z) = (0.01\lambda, 0.01\lambda, 0.01\lambda)$, and $\mathbf{\Lambda}(\boldsymbol{r}) = 1$. In the body of the figure the global coordinates of the observation point are reported in meters.

by Gautschi's integration of (10) is superior to the quality of the results obtained via Gauss-Legendre integration of (16). This is even more evident in the critical case considered in the right-hand side of Fig. 9, which shows that machine precision results can always be obtained by use of (10), whereas this does not happen when numerical integration is done using (16), particularly in the case of the quartic source densities $\mathbf{\Lambda}(\boldsymbol{r}) = x_T^4$ and $\mathbf{\Lambda}(\boldsymbol{r}) = y_T^4$. However, one should notice that elements of the size of one wavelength, such as $T_1$, are seldom used in numerical applications. The results of Fig. 9 show that Gautschi's integration with the number of samples reported in Tables IV and V can be employed with great confidence to numerically evaluate the non-displaced potentials of quartic sources over domains of size up to about one-third or one-half of a wavelength. In fact, in Fig. 9, machine precision results for $T_{10}$ are obtained with 6 $(= m_0 + 3)$ radial and 11 $(= n_0 + 6)$ transverse samples, whereas 9 radial $(= m_0 + 6)$ and 17 transverse $(= n_0 + 12)$ samples yield machine precision results for the triangle $T_1$.

We finally discuss results for dynamic near-singular potential integrals, with observation point displaced at a distance $d$ from the plane of the integration domain. In spite of the fact that *displaced* integrals are never singular, their numerical evaluation, also in the static limit (see Fig. 5), requires a higher number of radial points with respect to the number required to deal with the case of $d = 0$. As discussed in Section IV, this happens because the pole $\widetilde{\varphi}$ of the integral kernel is $\rho$-dependent for $d \neq 0$. In the dynamic case, the kernel of the integral also contains the exponential factor $\exp(-jkR)$, which requires a further increase in the number of radial and transverse samples. This is not surprising if one considers the expression of the distance $R$ from observation to integration point. For example, the normalized distance (6) is linear in $\rho$ if $d_k = 0$, that is for observation points located in the plane of the source domain, whereas it becomes a rather complex expression in $\rho$ and $\varphi$ (or $\Upsilon$) whenever $d_k \neq 0$. To deal with a displaced dynamic case one has to use much denser grids for *trigonometric* reasons, since one is actually faced with the problem of numerically representing the distance $R$ that appears in the factor $\exp(-jkR)$ in terms of an angle $\alpha$ that is a complicated function of the integration point coordinates, with $R = d/\cos\alpha$. The effect of the trigonometric problem is reduced by moving the observation point further off the plane of the source domain, and indeed the most difficult displaced dynamic integrals are obtained for very small, but non-vanishing $d$ values.

The results of Figs. 10 and 11 are relative to the convergence study of the nearly singular integral (5) over $T_{10}$, with $\lambda = 10$ [m] and observation point $(x, y, z) = (0.1, 0.1, d)$ [m], for $d = 0.1$ [m] (Fig. 10), and $d = 0.01$ [m] (Fig. 11). Fig. 10 considers the case of $\mathbf{\Lambda}(\boldsymbol{r}) = 1$, and $d = 0.01\lambda$. As stated, the Gautschi quadrature rule to integrate in $\varphi$ is $\rho$-dependent in this case, since the pole $\widetilde{\varphi}$ moves whenever $\rho$ is changed (see (11)). The same quadrature rule to integrate in $\varphi$ can be used for all $\rho \in [0, 1]$ only if the pole at $\varphi = \widetilde{\varphi}$ is $\rho$-invariant, as happens only in the non-displaced case of $d = 0$. However, we have also computed (5) by integrating (10), for all the 32 $\rho$-samples of Fig. 10, with the same Gautschi quadrature rule derived for the $\widetilde{\varphi}$ value one has in case of $d = 0$; the results obtained in this manner are labelled with triangles in Fig. 10. These results are reported just to show the possibility of reducing the computational burden of the Gautschi algorithm by assuming pole invariance on adjacent $\rho$-samples. The Duffy results of Fig. 10 were obtained by integrating (9) numerically, whereas the results labelled by squares (GL rational) were obtained by Gauss-Legendre integration of (10). It is of interest to observe the rather poor quality of the Duffy results; in fact, the quality of the results obtained by using a brutal simplification of the Gautschi scheme (i.e., the triangle-results) is superior to the Duffy one.

Fig. 11 was obtained by locating the observation point $(x, y, z) = (0.01\lambda, 0.01\lambda, 0.001\lambda)$ at a closer distance from the plane of the source domain, with respect to the distance used to get the results of Fig. 10. Therefore, to obtain machine precision results, we used $\rho$-grids much denser than that used in Fig. 10. The results for $\mathbf{\Lambda}(\boldsymbol{r}) = x_T^4$ are reported on the left side of Fig. 11, while the results on the right hand side were obtained for $\mathbf{\Lambda}(\boldsymbol{r}) = (1 - x_T - y_T)^4$. The number of radial samples to achieve convergence of the Gautschi results agrees with the number reported in Table IV; convergence of the results is obtained here with 11 $(= n_0 + 6)$ transverse samples, that is for $\Delta_n = 6$, again in agreement with Tables IV and V. Fig. 11 illustrates that usually the most difficult near-singular integrals are those relative to $\mathbf{\Lambda}$ functions of higher order that are significantly different from zero in the neighborhood of the normal projection of the observation point onto the plane of the source domain.

## VII. Conclusion

A new technique for machine precision evaluation of singular and nearly singular potentials integrals with $1/R$ singularities is presented. The quadrature scheme, based on the cancellation method, works for two- and three-dimensional integrals, and is developed in the parent reference frame of the integration domains by using, from the very beginning, the language and the techniques well known to finite element analysts. A detailed

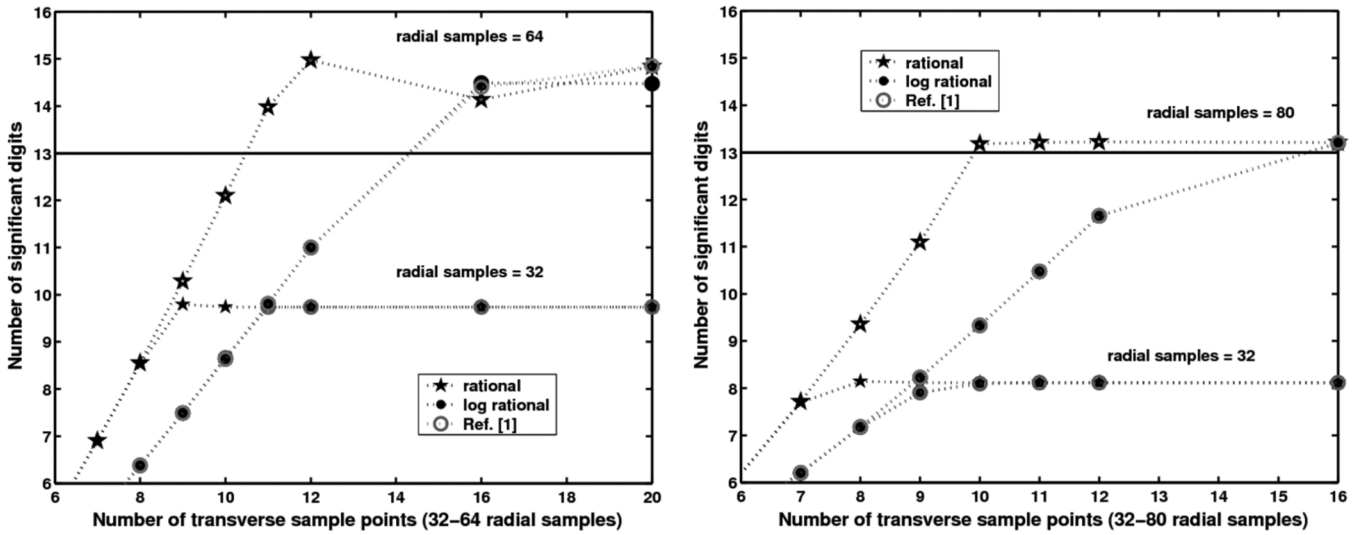



Fig. 11. Convergence comparison for a nearly singular integral over the triangle $T_{10}$, with observation point $(x, y, z) = (0.1, 0.1, 0.01)$ [m], $\mathbf{\Lambda}(\boldsymbol{r}) = x_T^4$ (at left), and $\mathbf{\Lambda}(\boldsymbol{r}) = (1 - x_T - y_T)^4$ (at right). The value of the distance $d$ in wavelength is $z = d = 10^{-3}\lambda$.

analysis of the reason why nearly singular integrals are often more difficult to evaluate than singular ones is provided. The most important feature of the scheme is that it exactly integrates the static potential of polynomial source distributions. The rules to achieve machine-precision accuracy in the static and dynamic case of 2D integrals are provided, and several numerical results for the triangular element are presented.

## Appendix I
## Transformation Formulas for Singularity Cancellation in the Parent Domain

As stated in Section III, for a given element of size $\sigma$, a potential integral on $\boldsymbol{\xi}$ over the element region $E_\xi$ is subdivided into $\sigma$ sub-integrals, with integral subdomains obtained by joining, in the parent space, a point $\boldsymbol{\xi}^\circ$ to each vertex of the parent domain (see Fig. 1). The variable transformation formulas are obtained by applying, in the parent space, the general four-step procedure described in the following paragraphs.

### A. Duplication of the Parent Set

Beside the parametric set $\boldsymbol{\xi}$, we introduce a second set $\boldsymbol{\Upsilon}$ of normalized coordinates having the same size as $\boldsymbol{\xi}$. The $\Upsilon$-parametric coordinates satisfy the same dependency relationships that hold for the $\xi$-coordinates, and the region $E_\Upsilon = \{\Upsilon_i | \Upsilon_i \geq 0, \forall i \in [1, \sigma]\}$ is a *copy* of the entire integration domain $E_\xi$; in other words, the two sets $\boldsymbol{\xi}$ and $\boldsymbol{\Upsilon}$ are equivalent except for the name given to the coordinates of each set.

### B. Introduction of the Pseudo-Radial Variable

We introduce a new parametric variable $\nu \geq 0$, and then append this variable to the duplicated set $\boldsymbol{\Upsilon}$ to form the new parametric set $\boldsymbol{\Upsilon}_\nu = (\Upsilon_1, \Upsilon_2, \ldots, \Upsilon_\sigma, \nu)$, with size equal to $\sigma + 1$.

### C. Radial-Binding at $\boldsymbol{\xi}^\circ$

We bind the $\boldsymbol{\xi}$ and the $\boldsymbol{\Upsilon}_\nu$ set together by setting

$$\xi_i = \xi_i^\circ (1 - \nu) + \nu \Upsilon_i, \text{ for } i = 1, 2, \ldots, \sigma \tag{29}$$

so to obtain, for all the allowed values of the integer subscript $i(= 1, \sigma)$

$$\begin{cases} \xi_i = \xi_i^\circ & \text{at } \nu = 0 \\ \xi_i = \Upsilon_i & \text{at } \nu = 1 \end{cases}. \tag{30}$$

The pseudo-radial variable $\nu$ binds the two sets together at $\boldsymbol{\xi}^\circ$ since, for $\nu \neq 0$, (29) requires $\Upsilon_i = \xi_i^\circ$ whenever $\xi_i = \xi_i^\circ$.

### D. Subdomain Selection via Zero-Blocking and Variable Transformation Formulas

By *blocking* to zero one $\Upsilon$-coordinate at a time of the augmented set $\boldsymbol{\Upsilon}_\nu$ one obtains $\sigma$ different sets of size $\sigma$ that are used together with (29) to subdivide the original parent domain into $\sigma$ subdomains. Only the *unblocked* coordinates can vary in a blocked set, although all the coordinates remain bounded by the dependency relationships duplicated in the first step A. The transformation formulas for integration on the $k$th subdomain via singularity cancellation are thus simply obtained by setting

$$\Upsilon_k = 0 \tag{31}$$

in (29), for $k = 1, 2, \ldots, \sigma$. The $k$th subdomain is mapped by the region $\{\nu \in [0, 1], \boldsymbol{\Upsilon} \in E_\Upsilon, \text{ with } \Upsilon_k = 0\}$. The coordinate-surface $\xi_k = 0$ bounds the $k$th subdomain as well as the entire parent element; hence, because of (29), (31) and the second of (30), this yields $\Upsilon_k = \xi_k = 0$ at $\nu = 1$.

### E. Transformation Jacobians

The Jacobians of the variable transformation formulas vanish at $\nu = 0$, where the parent integration point $\boldsymbol{\xi}$ coincides with $\boldsymbol{\xi}^\circ = (\xi_1^\circ, \xi_2^\circ, \ldots, \xi_\sigma^\circ)$; this is why $\nu$ is referred to as a pseudo-radial variable. In particular, for the $k$th subdomain selected by setting $\Upsilon_k = 0$, the Jacobian $\mathcal{J}_k$ becomes $\mathcal{J}_k = \xi_k^\circ \nu$ in case of 2D elements whereas, for 3D-elements, one has $\mathcal{J}_k = \xi_k^\circ \nu^2$.

## Appendix II
## Study of the Essential Singularity of the Exponential Factor Appearing in (10)

For the kernel of (10), it is of importance to study the behavior of the exponential factor as a function of the new integration variables $(\rho, \varphi)$. The distance $R$ reads

$$R = \frac{-\widetilde{\varphi}}{\varphi - \widetilde{\varphi}} \ell_k f(\rho, \varphi) \geq 0 \tag{32}$$

with

$$\lim_{\rho \to 0} R = \ell_k d_k = d, \quad \forall \varphi \tag{33}$$

and where $f(\rho, \varphi)$ is an irrational algebraic function that is equal to $d_k$ in the limit $\rho \to 0$. The basis function $\boldsymbol{\Lambda}$ in (10) is actually computed in terms of the parent or of the object-space coordinates, which are easily obtained by sequentially mapping the given integration point $(\rho, \varphi)$ backward into the corresponding point of the $(\rho, \Upsilon)$-space, then into the point $\boldsymbol{\xi}$ of the parent-space, and finally into the point $\boldsymbol{r}'$ of the global space. The expression for $f(\rho, \varphi)$ is not reported because the backward mapping already done for $\boldsymbol{\Lambda}$ makes it more convenient to evaluate the distance $R = |\boldsymbol{r} - \boldsymbol{r}'|$ directly in the object-space, without using (32). However, (32) and (33) are important and deserve further discussion. We first observe that (33) and (6) coincide at $\rho = 0$, whereas one needs to separately consider the cases of $d_k = 0$ and $d_k \neq 0$ in order to prove (33) by starting with (32). In fact, for $d_k = 0$, $\widetilde{\varphi}$ is $\rho$-invariant and (32) simplifies into (13). Conversely, for $d_k \neq 0$, (11) implies $\widetilde{\varphi} \to -\infty$ in the limit $\rho \to 0$, with a corresponding distance $R$ that becomes approximately equal to $\ell_k f(\rho, \varphi)$ at very small $\rho$ values. Since $f(\rho, \varphi)$ never vanishes at $\varphi = \widetilde{\varphi}$, unless $d_k$ and $\rho$ are zero,

$$f(\rho, \widetilde{\varphi}) = (1 - \widetilde{\varphi})\,[r(\rho, 0) - C_k] \tag{34}$$

$$\lim_{\rho \to 0} f(\rho, \widetilde{\varphi}) = d_k \tag{35}$$

equations (32) and (33) clearly show that $R$ has a real-negative pole at $\varphi = \widetilde{\varphi}$, and that the pole vanishes in the limit for $\rho = 0$. At the same time, the exponential factor $\exp(-jkR)$ exhibits an essential singularity at $\varphi = \widetilde{\varphi}$ which vanishes in the limit for $\rho = 0$. In spite of this, recall that the kernel of (10) always exhibits a pole at $\varphi = \widetilde{\varphi}$, also in the limit for $\rho = 0$. The effect of the essential singularity of the exponential factor over the integration interval $\varphi \in [0, 1]$ is mitigated by the fact that $\widetilde{\varphi}$ is always outside the integration interval, and also because of the special form of (13) and (32), which contain the pole-term $1/(\varphi - \widetilde{\varphi})$ multiplied by the factor $\widetilde{\varphi}$. The singularities of $R$ and of the exponential factor are indeed weakened by decreasing the value of $\rho \in [0, 1]$, and they disappear at $\rho = 0$ as reported in (33). As a matter of fact, in spite of the singularity, one can numerically prove that the truncated series that follows converges rapidly for all $\varphi \in [0, 1]$, and for constant $\rho \in [0, 1]$

$$\frac{\exp(-jkR)}{(\varphi - \widetilde{\varphi})} \simeq \frac{a_0}{(\varphi - \widetilde{\varphi})} + \frac{a_1 \widetilde{\varphi}}{(\varphi - \widetilde{\varphi})^2} + \cdots + \frac{a_N \widetilde{\varphi}^N}{(\varphi - \widetilde{\varphi})^{N+1}} \tag{36}$$

$$a_n = \frac{[jk\ell_k f(\rho, \varphi)]^n}{n!} \tag{37}$$

though, as previously stated, (13), (32) and (36) are never used to evaluate (10) numerically.

## Appendix III
## Transformation Formulas for 3D Elements

Table II summarizes the results obtained by subdividing the most common 3D-element geometries about the parent-point $\boldsymbol{\xi}^\circ$, according to the procedure described in Appendix I. Recall that the procedure aims at dealing with hyper-straight elements for which the straight lines that subdivide the parent element are mapped by (2) into straight lines that join the observation point $\boldsymbol{r}$ to the vertices of the object element. The case of the pyramidal element in the last row of Table II is therefore considered only for the sake of completeness, since the pyramidal element discussed in [30] is not hyper-straight. In order to deal with a non hyper-straight element, one must first subdivide the object element into sub-tetrahedrons and then re-parameterize each object subdomain before using the proper result of Table II.

All the elements of Table II are split into sub-tetrahedrons and/or into square-based sub-pyramids, and $\boldsymbol{\xi}^\circ$ is the common tip of all the sub-pyramids/sub-tetrahedrons associated with a given element. Each subdomain retains only one face of the original element, which in Table II is understood to be the $\xi_k = 0$ face, and inherits the local order number of the element face that backs up the subdomain itself. The $k$th subdomain is therefore the only one bounded by the $k$th face of the entire element. For example, the $k$th face of the prism of Fig. 4 (at left) is a quadrilateral and the $k$th subdomain based on this face is a pyramid, while for the $k$th triangular face of the tetrahedron shown at right the $k$th subdomain backed up by this face is a tetrahedron.

Subdomain integration can be performed by integrating first on layers parallel to the retained $\xi_k = 0$ face and then along the pseudo-radial $\nu$-direction. With this observation in mind, we *iterate the procedure* and further subdivide the subdomains of Table II by means of (3) and (4).

By cutting the $k$th subdomain with a sheaf of planes parallel to the $k$th element's face (the parametric equation of these planes is $\nu = const.$, with $0 \leq \nu \leq 1$) we subdivide the sub-pyramids and the subtetrahedrons into layers of quadrilaterals and triangles, respectively. For example, the subpyramid at left in Fig. 4 has a stack of three quadrilaterals, and the subtetrahedron at right has a stack of three triangles. In the global space, the straight line $t_k$ is drawn to normally project the observation point $\boldsymbol{r}$ onto the parallel layers of the $k$th subdomain, $\boldsymbol{r}_k$ is the normal projection of $\boldsymbol{r}$ onto the $k$th element face, and $\ell_{ka}$ is the length of the edge $ka$ common to the $k$th and $a$th element face. The dummy index $a$ is specified as reported in Table II, and it stands for $\ell$, $m$, or $n$ when dealing with a sub-tetrahedron, or for $p$, $q$, $s$, or $t$ when dealing with a sub-pyramid.

Fig. 4 shows that the observation point $\boldsymbol{r}$ is the center of similarity transformations. These transformations multiply all distances of the $k$th subdomain by $\nu$, with $\nu = 0$ at $\boldsymbol{r}$, and $\nu = 1$ for all points lying on face $k$ opposite to the observation point. As shown at the bottom of Fig. 4, the normal projections of the observation point $\boldsymbol{r}$ onto all layers of the $k$th stack coincide into one point in the bottom-view of the $k$th subdomain. That is to say that the parent normalized coordinates of the normal projections are the same for all the quadrilaterals or triangles of the stack. In the following, the parent coordinates of these normal projections are $\{\xi_\ell = \zeta_{k\ell}, \xi_m = \zeta_{km}, \xi_n = \zeta_{kn}\}$ for the $k$th tetrahedral subdomain whereas, for pyramidal subdomains, the parent coordinates of the normal projections are $\{\xi_p = \zeta_{kp}, \xi_q = \zeta_{kq}, \xi_s = \zeta_{ks}, \xi_t = \zeta_{kt}\}$. The above observation is of importance for integrating by a change of variables on layers parallel to the $k$th face, thereby transforming the $\xi$-parent coordinates by use of Table II and then by use of formulas (38)–(41), reported below. To perform the latter change of variables, one needs to calculate only the parent coordinates of the normal projection $\boldsymbol{r}_k$, since the parent coordinates of the normal projection on all the quadrilateral or triangular parallel layers do not change. As a matter of fact, a 3D element is broken into subdomains to ultimately subdivide, about the line $t_k$, the stack of layers relative to the $k$th tetrahedral (or pyramidal) subdomain into three (or four) stacks of sub-triangles. Obviously, the same result could be obtained by subdividing first about the line $t_k$ the $k$th subdomain into three (or four) subtetrahedrons that retain only one edge of the $k$th face of the original 3D element, and then cut the sub-tetrahedrons obtained in this manner with a sheaf of $\nu = const.$ planes.

It is now plain that one integral over a tetrahedral subdomain of Table II is actually decomposed into three volumetric sub-integrals. The new variable transformation formulas associated with these sub-integrals are obtained directly from (3) by re-defining, in three different ways (one per sub-subdomain), the variables $\xi_\ell$, $\xi_m$ and $\xi_n$ of the central column of Table II. To do this we select the point with parent coordinates $\{\xi_k = 0, \xi_\ell = \zeta_{k\ell}, \xi_m = \zeta_{km}, \xi_n = \zeta_{kn}\}$ of the $k$th surface. Recall that this point is obtained by *projecting* the observation point $\boldsymbol{r}$ of parent coordinates $(\xi_1^\circ, \xi_2^\circ, \ldots, \xi_\sigma^\circ)$ onto the object-domain surface $\xi_k = 0$. Since $\zeta_{k\ell} + \zeta_{km} + \zeta_{kn} = 1$, (3) yields

$$\begin{aligned} \Upsilon_a &= \zeta_{ka}(1-\rho) \\ \Upsilon_b &= \zeta_{kb}(1-\rho) + \rho\Upsilon \\ \Upsilon_c &= \zeta_{kc}(1-\rho) + \rho(1-\Upsilon) \end{aligned} \tag{38}$$

where the dummy subscripts $a$, $b$, and $c$ are in turn given by one of the following three cyclic permutations of the $\ell$, $m$, $n$ subscripts of Table II

$$\{a,b,c\} = \begin{cases} \{\ell,m,n\} \\ \{n,\ell,m\} \\ \{m,n,\ell\} \end{cases} \tag{39}$$

so that one has $\Upsilon_a + \Upsilon_b + \Upsilon_c = 1$. The three sets of sub-subtetrahedron transformation formulas are then obtained by substituting (38), (39) into the transformation formulas for $\xi_\ell$, $\xi_m$ and $\xi_n$ given at top of Table II. These transformations map each sub-subtetrahedron into the cube-shaped region $\{0 \le \nu \le 1, 0 \le \rho \le 1, 0 \le \Upsilon \le 1\}$. The Jacobian $\mathcal{J}_{ka} = (\zeta_{ka}\xi_k^\circ \nu^2 \rho)$ of these transformations (for $a = \ell$, $m$, or $n$) has a first- and a second-order zero at $\rho = 0$ and at $\nu = 0$, respectively.

Similarly, the sub-pyramid associated with the $k$th quadrilateral face of a given original element of Table II is subdivided into four sub-subtetrahedrons that retain only one edge of the original element by selecting, on the $k$th surface ($\xi_k = 0$), the parent point $\{\xi_k = 0, \xi_p = \zeta_{kp}, \xi_q = \zeta_{kq}, \xi_s = \zeta_{ks}, \xi_t = \zeta_{kt}\}$, with $\zeta_{kp} + \zeta_{kq} = 1$ and $\zeta_{ks} + \zeta_{kt} = 1$. Use of (4) yields

$$\begin{aligned} \Upsilon_a &= \zeta_{ka}(1-\rho) \\ \Upsilon_b &= \zeta_{kb}(1-\rho) + \rho \\ \Upsilon_c &= \zeta_{kc}(1-\rho) + \rho\Upsilon \\ \Upsilon_d &= \zeta_{kd}(1-\rho) + \rho(1-\Upsilon) \end{aligned} \tag{40}$$

where the dummy $a$, $b$, $c$ and $d$ subscripts are given by one of the following four permutations of the $p$, $q$, $s$, $t$ subscripts

$$\{a,b,c,d\} = \begin{cases} \{p,q,s,t\} \\ \{s,t,q,p\} \\ \{q,p,t,s\} \\ \{t,s,p,q\} \end{cases} \tag{41}$$

that yield $\Upsilon_a + \Upsilon_b = 1$ and $\Upsilon_c + \Upsilon_d = 1$. Four sets of transformation formulas are then obtained by substituting (40), (41) into the expressions of $\xi_p$, $\xi_q$, $\xi_s$ and $\xi_t$ reported at top of Table II. These transformations map each of the four sub-subtetrahedrons into the cube-shaped region $\{0 \le \nu \le 1, 0 \le \rho \le 1, 0 \le \Upsilon \le 1\}$. Once again, the Jacobian $\mathcal{J}_{ka} = (\zeta_{ka}\xi_k^\circ \nu^2 \rho)$ of these transformations (for $a = p$, $q$, $s$ or $t$) has first- and second-order zeroes at $\rho = 0$ and at $\nu = 0$, respectively.

## ACKNOWLEDGMENT

The authors are grateful to D. R. Wilton of the University of Houston for providing the numerical integration code described in [1], and for the valuable subject related discussions while he was a Visiting Scholar at the Polytechnic of Turin, Italy.

## REFERENCES

[1] M. A. Khayat and D. R. Wilton, "Numerical evaluation of singular and near-singular potential integrals," *IEEE Trans. Antennas Propag.*, vol. 53, pp. 3180–3190, Oct. 2005.

[2] D. M. Tracey, "Finite elements for determination of crack tip elastic stress intensity factors," *Eng. Fracture Mechan.*, vol. 3, no. 3, pp. 225–265, 1971.

[3] M. Stern and E. B. Becker, "A conforming crack tip element with quadratic variation in the singular fields," *Int. J. Numer. Methods Eng.*, vol. 12, pp. 279–288, 1978.

[4] M. G. Duffy, "Quadrature over a pyramid or cube of integrands with a singularity at a vertex," *SIAM J. Numer. Anal.*, vol. 19, no. 6, pp. 1260–1262, 1982.

[5] R. D. Graglia, "Static and dynamic potential integrals for linearly varying source distributions in two- and three-dimensional problems," *IEEE Trans. Antennas Propag.*, vol. AP-35, pp. 662–669, Jun. 1987.

[6] W. Hackbusch and S. A. Sauter, "On numerical cubatures of nearly singular surface integrals arising in BEM collocation," *Computing*, vol. 52, no. 2, pp. 139–159, 1994.

[7] W. Hackbusch, *Integral Equations. Theory and Numerical Treatment*. Basel, Germany: Birkhäuser Verlag, 1995, vol. 120, International Series of Numerical Mathematics.

[8] P. R. Johnston and D. Elliott, "A sinh transformation for evaluating nearly singular boundary element integrals," *Int. J. Numer. Methods Eng.*, vol. 62, pp. 564–578, 2005.

[9] B. M. Johnston, P. R. Johnston, and D. Elliott, "A sinh transformation for evaluating two-dimensional nearly singular boundary element integrals," *Int. J. Numer. Methods Eng.*, vol. 69, pp. 1460–1479, 2007.
[10] D. R. Wilton, S. M. Rao, A. W. Glisson, D. H. Schaubert, O. M. Al-Bundak, and C. M. Butler, "Potential integrals for uniform and linear source distributions on polygonal and polyhedral domains," *IEEE Trans. Antennas Propag.*, vol. 32, pp. 276–281, Mar. 1984.
[11] R. D. Graglia, "The use of parametric elements in the moment method solution of static and dynamic volume integral equations," *IEEE Trans. Antennas Propag.*, vol. AP-36, no. 5, pp. 636–646, May 1988.
[12] R. D. Graglia, P. L. E. Uslenghi, and R. S. Zich, "Moment method with isoparametric elements for three-dimensional anisotropic scatterers," *Proc. IEEE—Special Issue on Radar Cross Sections of Complex Objects*, vol. 77, no. .5, pp. 750–760, May 1989.
[13] L. Knockaert, "A general Gauss theorem for evaluating singular integrals over polyhedral domains," *Electromagn.*, vol. 11, pp. 269–280, 1991.
[14] R. D. Graglia, "On the numerical integration of the linear shape functions times the 3-D Green's function or its gradient on a plane triangle," *IEEE Trans. Antennas Propag.*, vol. 41, pp. 1448–1456, Oct. 1993.
[15] T. F. Eibert and V. Hansen, "On the calculation of potential integrals for linear source distributions on triangular domains," *IEEE Trans. Antennas Propag.*, vol. 43, pp. 1499–1502, Dec. 1995.
[16] D. Sievers, T. F. Eibert, and V. Hansen, "Correction to: On the calculation of potential integrals for linear source distributions on triangular domains," *IEEE Trans. Antennas Propag.*, vol. 53, no. 9, p. 3113, Sept. 2005.
[17] B. M. Notaros and B. D. Popovic, "Optimized entire-domain moment-method analysis of 3D dielectrics scatterers," *Int. J. Numer. Model.*, vol. 10, pp. 177–192, 1997.
[18] L. Rossi and P. J. Cullen, "On the fully numerical evaluation of the linear-shape function times the 3-D Green's function on a plane triangle," *IEEE Trans. Microw. Theory Tech.*, vol. 47, pp. 398–402, Apr. 1999.
[19] S. Järvenpää, M. Taskinen, and P. Ylä-Oijala, "Singularity extraction technique for integral equation methods with higher order basis functions on plane triangles and tetrahedra," *Int. J. Numer. Meth. Eng.*, vol. 58, pp. 1149–1165, Aug. 2003.
[20] S. Caorsi, D. Moreno, and F. Sidoti, "Theoretical and numerical treatment of surface integrals involving the free-space Green's function," *IEEE Trans. Antennas Propag.*, vol. 41, no. 9, pp. 1296–1301, Sep. 1993.
[21] D. Rosen and D. E. Cormack, "The continuation approach: A general framework for the analysis and evaluation of singular and near-singular integrals," *SIAM J. Appl. Math.*, vol. 55, no. 3, pp. 723–762, 1995.
[22] J. T. Beale and M. Lai, "A method for computing nearly singular integrals," *SIAM J. Numer. Anal.*, vol. 38, no. 6, pp. 1902–1925, 2001.
[23] J. M. Jin, *The Finite Element Method in Electromagnetics*, 2nd ed. New York: Wiley, 2002.
[24] W. Gautschi, "Algorithm 793: GQRAT-Gauss Quadrature for Rational Functions," *ACM Trans. Math. Softw.* vol. 25, no. 2, pp. 213–239, 1999 [Online]. Available: http://www.doi.acm.org/10.1145/317275.317282
[25] G. Lombardi and R. D. Graglia, "Accurate evaluation of potential integrals with Gauss quadrature formulas for rational functions," in *Proc. IEEE AP-S Int. Symp.*, Honolulu, HI, Jun. 2007, pp. 4841–4844.
[26] R. D. Graglia and G. Lombardi, "Exact quadrature of singular and nearly singular potential integrals," in *Proc. Int. Conf. on Electromagnetics in Advanced Applications (ICEAA'07)*, Torino, Italy, Sep. 2007, pp. 982–985.
[27] J. C. Nédélec, "Mixed finite element in $\mathrm{R}^3$," *Numerische Mathematik*, vol. 35, pp. 315–341, 1980.
[28] R. D. Graglia, D. R. Wilton, and A. F. Peterson, "Higher order interpolatory vector bases for computational electromagnetics," *IEEE Trans. Antennas Propag. Special Issue on Advanced Numerical Techniques in Electromagnetics*, vol. 45, no. 3, pp. 329–342, Mar. 1997.
[29] R. D. Graglia, D. R. Wilton, A. F. Peterson, and I.-L. Gheorma, "Higher order interpolatory vector bases on prism elements," *IEEE Trans. Antennas Propag.*, vol. 46, no. 3, pp. 442–450, Mar. 1998.
[30] R. D. Graglia and I.-L. Gheorma, "Higher order interpolatory vector bases on pyramidal elements," *IEEE Trans. Antennas Propag.*, vol. 47, no. 5, pp. 775–782, May 1999.
[31] I. S. Gradshteyn and I. M. Ryzhik, *Table of Integrals, Series, and Products*. New York: Academic Press, Inc., 1980.
[32] A. H. Stroud and D. Secrest, *Gaussian Quadrature Formulas*. Englewood Cliffs, NJ: Prentice-Hall, 1966.
[33] D. A. Dunavant, "High degree efficient symmetrical Gaussian quadrature rules for the triangle," *Int. J. Numer. Methods Eng.*, vol. 21, no. 6, pp. 1129–1148, 1985.



**Roberto D. Graglia** (S'83–M'83–SM'90–F'98) was born in Turin, Italy, on July 6, 1955. He received the Laurea degree (*summa cum laude*) in electronic engineering from the Polytechnic of Turin, in 1979, and the Ph.D. degree in electrical engineering and computer science from the University of Illinois at Chicago, in 1983.

From 1980 to 1981, he was a Research Engineer at CSELT, Italy, where he conducted research on microstrip circuits. From 1981 to 1983, he was a Teaching and Research Assistant at the University of Illinois at Chicago. From 1985 to 1992, he was a Researcher with the Italian National Research Council (CNR), where he supervised international research projects. In 1991 and 1993, he was Associate Visiting Professor at the University of Illinois at Chicago. In 1992, he joined the Department of Electronics, Polytechnic of Turin, as an Associate Professor. He has been a Professor of Electrical Engineering at that Department since 1999. He is also with the ISMB-Instituto Superiore Mario Boella, Torino, Italy. He has authored over 150 publications in international scientific journals and symposia proceedings. His areas of interest comprise numerical methods for high- and low-frequency electromagnetics, theoretical and computational aspects of scattering and interactions with complex media, waveguides, antennas, electromagnetic compatibility, and low-frequency phenomena. He has organized and offered several short courses in these areas.

Dr. Graglia has been a Member of the editorial board of *Electromagnetics* since 1997. He is a past Associate Editor of the IEEE TRANSACTIONS ON ANTENNAS AND PROPAGATION and the IEEE TRANSACTIONS ON ELECTROMAGNETIC COMPATIBILITY. He is currently an Associate Editor of the IEEE ANTENNAS AND WIRELESS PROPAGATION LETTERS, and a Reviewer for several international journals. He was the Guest Editor of a Special Issue on Advanced Numerical Techniques in Electromagnetics for the IEEE TRANSACTIONS ON ANTENNAS AND PROPAGATION in March 1997. He has been Invited Convener at URSI General Assemblies for special sessions on Field and Waves in 1996, Electromagnetic Metrology in 1999, and Computational Electromagnetics in 1999. He served the International Union of Radio Science (URSI) for the triennial International Symposia on Electromagnetic Theory as Organizer of the Special Session on Electromagnetic Compatibility in 1998 and was the co-organizer of the special session on Numerical Methods in 2004. Since 1999, he has been the General Chairperson of the biennial International Conference on Electromagnetics in Advanced Applications (ICEAA), held in Turin. He is presently serving the IEEE Antennas and Propagation Society as a member of AdCom, for the triennium 2006–2008.



**Guido Lombardi** (S'02–M'03) was born in Florence, Italy, on December 8, 1974. He received the Laurea degree (*summa cum laude*) in telecommunications engineering from the University of Florence, Florence, Italy, in 1999, and the Ph.D. degree in electronics engineering from the Polytechnic of Turin, Turin, Italy, in January 2004. His Ph.D. work focused on the study of analytical and numerical aspects of electromagnetic singularities.

From 2000 to 2001, he was an Officer of the Italian Air Force. In 2004, he joined the Department of Electronics, Polytechnic of Turin, as an Associate Researcher. He has been an Assistant Professor at that Department since 2005. His research areas comprise numerical methods for electromagnetics, theoretical and computational aspects of FEM and MoM, Wiener-Hopf method, electromagnetic singularities, waveguide problems, microwave passive components and project of orthomode transducers (OMT).

Dr. Lombardi received the Raj Mittra Travel Grant Award, as a Junior Researcher, at the 2003 IEEE AP-S International Symposium and USNC/CNC/URSI National Radio Science Meeting, Columbus, OH. In the same year he spent two months as Research Visitor at the Department of Electrical and Computer Engineering, University of Houston, Houston, TX. Since 2001, he served as a member of the Organizing Committee of the biennial International Conference on Electromagnetics in Advanced Applications (ICEAA), held in Turin. He is currently a Reviewer for several international journals.